NUMERICAL MODELLING OF TRANSIENT UNDER-EXPANDED JETS UNDER DIFFERENT AMBIENT THERMODYNAMIC CONDITIONS WITH ADAPTIVE MESH REFINEMENT

A. Hamzehloo and P.G. Aleiferis*

Department of Mechanical Engineering, Imperial College London, UK

*Author for Correspondence:

Prof. Pavlos Aleiferis

Imperial College London

Department of Mechanical Engineering

Exhibition Road, London SW7 2AZ, UK

Tel: +44-(0)20-75947032

E-mail: p.aleiferis@imperial.ac.uk

Full length article accepted for publication in the International Journal of Heat and Fluid Flow

Abstract

The mixing characteristics of highly turbulent under-expanded gaseous fuel jets issued from millimeter-size circular nozzles are important for developing advanced direct injection gaseous-fuelled internal combustion engines. In the present study high-resolution large eddy simulation in conjunction with an adaptive mesh refinement technique was used in order to investigate key mixing characteristics of under-expanded hydrogen and methane jets under various ambient thermodynamics. Penetration rate, volumetric growth and initial transient vortex ring behaviour were investigated under near atmospheric and elevated ambient pressures and temperatures, $P_\infty \approx 1$ bar and 10 bar, $T_\infty = 296$ K and 600 K, using a nozzle pressure ratio of 10. The conditions corresponded to injection strategies ranging from late intake stroke around inlet valve closure to late compression. It was observed that increasing the ambient temperature at constant pressure resulted in increase in both tip penetration and volumetric growth of the under-expanded jets. It was also found that the effect of diffusivity, ratio of specific heats and ambient density must be considered when scaling volumetric growth of under-expanded jets of different gases and/or when issued into different ambient temperatures. Moreover, substantial differences were observed between the transient jet formation of hydrogen and methane fuels. It was found that the embedded shock structures and supersonic annular shear layers played a significant role in the formation and evolution of the transient preliminary and secondary vortex rings. It was also noted that the evolution of the vortex ring influenced significantly the volumetric growth and hence mixing quality of under-expanded jets.

Keywords:

Under-expanded Jet, Vortex ring, Shear layer, *Mach* disk, Reflected shock, Turbulent mixing, Adaptive mesh.

1. Introduction

Powering internal combustion (IC) engines with hydrogen or methane gas is one of the proposed resolutions to diversify progressively towards use of cleaner energy carriers particularly for the transportation sector (Cho and He, 2007; Verhelst, 2014). Direct injection (DI) of fuels into the combustion chamber is believed to be the most appropriate fuelling approach for advanced gaseous-fuelled IC engines. This is because DI can deliver relatively high volumetric efficiency when compared to port fuel injection and also provides extensive flexibility in controlling the air/fuel mixture homogeneity and stratification through a broad range of injection strategies (Scarcelli *et al.*, 2011; Hamzehloo and Aleiferis, 2013; Hamzehloo and Aleiferis, 2014a). High injection pressures are typically used for gaseous DI fuelling in order to achieve the required mass flow rates and promote air/fuel mixing (Hamzehloo and Aleiferis, 2013; Hamzehloo and Aleiferis, 2014a).

High injection pressures normally lead to the formation of highly under-expanded jets past the nozzle exit of gaseous fuel injectors (Scarcelli *et al.*, 2011; Hamzehloo and Aleiferis, 2013). The main characteristics of a gaseous jet injected from a circular nozzle are mainly affected by the ratio of the upstream (nozzle) total pressure (P_0) to the ambient (combustion chamber) static pressure (P_∞), the nozzle pressure ratio NPR=P_0/P_∞. Gaseous jets are normally categorized as subsonic, moderately under-expanded and highly under-expanded depending on their NPR level (Donaldson and Snedeker, 1971). The jets are typically considered to be highly under-expanded for NPR≥4 (Donaldson and Snedeker, 1971). At such conditions, *Mach* reflection occurs a few diameters downstream of the nozzle exit and forms a slightly curved strong normal shock, called the *Mach* disk (Donaldson and Snedeker, 1971; Vuorinen *et al.*, 2013; Hamzehloo and Aleiferis, 2014b). The distance of the *Mach* disk from the nozzle exit, *i.e.* the *Mach* disk height, and its respective width, are both strongly affected by NPR. A transient under-expanded jet contains a three-dimensional vortex ring which in addition to the *Mach* reflection contributes to the formation of three-dimensional annular shear layers (Golub, 1994; Edgington-Mitchell *et al.*, 2014). Vortex breakdown and/or vortex merging within these shear layers promotes mixing of the jet with the ambient medium (Krothapalli *et al.*, 1998). As a result, fundamental understanding of the aforementioned vortical structures of transient hydrogen and methane under-expanded jets is necessary in order to shed more light on the mixing characteristics of alternative gaseous fuels.

Various experimental and computational works have been devoted to under-expanded jets, using predominantly air or nitrogen issued from large diameter nozzles, mainly for aerospace applications. Recently, studies were conducted on under-expanded jets injecting from comparable nozzle diameters to those of typical gaseous IC engine injectors (D≤2.0 mm) (Vuorinen *et al.*, 2013; Yu *et al.*, 2013; Vuorinen *et al.*, 2014). The latter studies used large eddy simulation (LES) but were mainly limited to relatively low NPR values (NPR≤8) and to gases with fairly low diffusivity and/or speed of sound such as air, nitrogen and methane. This is due to the fact that high NPR values and/or gases with high diffusivity and speed of sound (such as hydrogen or helium) form relatively wide transient vortex rings and ‘bulky’ jets that require a fairly large number of computational elements for high-fidelity LES. Adaptive mesh refinement (AMR) is a

possible solution to control the number of computational cells over the solution domain and has been employed successfully for various applications. However, with respect to under-expanded jets, very limited computational studies are available on the basis of AMR (Prudhomme and Haj-Hariri, 1994; Zhang *et al.*, 2014). The present work aims to extend the previous studies of the current authors on under-expanded jets (Hamzehloo and Aleiferis, 2014b; Hamzehloo and Aleiferis, 2014c) by:

- Reporting on the development of a fully automated adaptive mesh refinement technique within the computational framework of STAR-CCM+ using Java user coding specifically for under-expanded jets.
- Performing direct comparison between the key mixing characteristics of under-expanded hydrogen and methane jets under near atmospheric and elevated ambient pressures and temperatures, $P_\infty \approx 1$ bar and 10 bar, T_∞=296 K and 600 K. The conditions corresponded to injection strategies ranging from late intake stroke around inlet valve closure to late compression.

To the author's best knowledge the present work is the first to use LES with AMR in order to discuss the characteristic behaviour of hydrogen and methane fuel jets under engine-like conditions of ambient pressure and temperature.

2. Methodology

2.1 Computational framework

The main aspects of the numerical methodology employed in order to conduct the present LES study within STAR-CCM+ have been discussed previously by the current authors (Hamzehloo and Aleiferis, 2014b; Hamzehloo and Aleiferis, 2014c, Hamzehloo and Aleiferis, 2016a). Nevertheless, for the immediate benefit of the reader, a brief description is also included here.

The governing equations of a multi-species viscous compressible flow, *i.e.* the equations that describe the conservation of mass, momentum and energy (equations 1–3), as well as an equation to model the transport of species (equation 4), are listed as follows (Ferziger and Peric, 2002):

$$\frac{\partial \rho}{\partial t} + \nabla \bullet (\rho \mathbf{U}) = 0 \tag{1}$$

$$\frac{\partial (\rho \mathbf{U})}{\partial t} + \nabla \bullet [\mathbf{U}(\rho \mathbf{U})] + \nabla p - \nabla \bullet \boldsymbol{\sigma} = 0 \tag{2}$$

$$\frac{\partial (\rho E)}{\partial t} + \nabla \bullet [\mathbf{U}(\rho E)] + \nabla \bullet (\mathbf{U} p) - \nabla \bullet (\boldsymbol{\sigma} \bullet \mathbf{U}) + \nabla \bullet \mathbf{q} = 0 \tag{3}$$

$$\frac{\partial (\rho Y_i)}{\partial t} + \nabla \bullet \rho \mathbf{U} Y_i = \nabla \bullet (\rho D_i \nabla Y_i) \tag{4}$$

where ρ is density, $\mathbf{U}$ represents the velocity vector $\mathbf{U}(u_i, u_j, u_k)$, p is pressure, $\boldsymbol{\sigma}$ is the Cauchy stress tensor that if the fluid is assumed to obey Newton's law of viscosity can be written as: $\boldsymbol{\sigma} = \mu[\nabla \mathbf{U} + (\nabla \mathbf{U})^{\mathrm{T}}] -$

$\left(\frac{2}{3}\mu\nabla \bullet \mathbf{U}\right)\mathbf{I}$ where T is the matrix transpose operator, μ is the dynamic viscosity and **I** is the identity tensor. In a Cartesian coordinate **σ** can be written as:

$$\sigma_{ij} = 2\mu S_{ij} - \frac{2}{3}\mu\delta_{ij}S_{kk} \tag{5}$$

where $S_{ij} = \frac{1}{2}\left(\frac{\partial u_i}{\partial x_j} + \frac{\partial u_j}{\partial x_i}\right)$ and δ_{ij} is the Kronecker's delta. $E = e + \frac{1}{2}|\mathbf{U}|^2$ is the total specific energy ($e = e(T, p)$ is the internal energy per unit mass, $|\mathbf{U}| = (\mathbf{U} \bullet \mathbf{U})^{1/2}$ is the magnitude of the velocity vector), $\mathbf{q} = \lambda\nabla T$ is the heat flux vector (T is the fluid temperature and λ is a heat conduction coefficient based on the Fourier law of heat conduction). For a calorically perfect compressible gas pressure and density are coupled using an equation of state as $p = \rho RT$, where R is the specific gas constant. Moreover, $e = C_v T$ and $R = C_p - C_v$, where C_v and C_p are the specific heat coefficients for constant volume and pressure, respectively. The aforementioned heat conduction coefficient may be defined using the molecular *Prandtl* number (Pr) as $\lambda = {C_p\mu}/{Pr}$. The mass fraction of species i^{th} is denoted by Y_i with a molecular diffusion coefficients of D_i. For N species, N-1 transport equations are solved and the mass fraction of the N^{th} component is calculated from the restriction that the total mass fraction must sum to unity.

In a turbulent flow (like an under-expanded jet) equation 1–4 are only valid within the *Kolmogorov* scales (*i.e.* direct numerical simulation (DNS) limit) in which the spatial and temporal resolutions are fine enough to capture all scales of the flow (Pope, 2000). However, at the present time conducting DNS on complex fluid flows and specifically on complex computational domains is not computationally practical due to the technological restriction (high computational costs). In the current study LES was employed in which the governing equations are filtered so that turbulence scales greater than a filter size (typically associated with the grid resolution but not necessarily) are resolved directly and the effect of scales smaller than that are accounted for by means of a subgrid-scale (SGS) modelling approach (Pope, 2000). Using the Favre averaging and applying the LES filtering to the momentum and energy conservation equations results in formation of residual-stress tensor due to the existence of non-liner terms (Pope, 2000). The residual-stress tensor τ_{ij}^R is defined as:

$$\tau_{ij}^R = \bar{\bar{\rho}}\left(\widetilde{u_i u_j} - \tilde{u}_i\tilde{u}_j\right) \tag{6}$$

where $\bar{\bar{\rho}}$ denotes the filtered density and ~ represents a *Favre*-averaged quantity. The anisotropic part of the residual-stress tensor is defined as:

$$\tau_{ij}^r = \tau_{ij}^R - \frac{2}{3}\mathrm{k}_r\delta_{ij} \tag{7}$$

where k_r is the residual kinetic energy defined as $\mathrm{k}_r \equiv \frac{1}{2}\tau_{ii}^R$.

In order to form a determined set of governing equations a *Boussinesq* type hypothesis may be used in order to model the anisotropic part of the residual stress tensor as (Pope, 2000):

$$\tau_{ij}^{r} = -\mathbf{2}\bar{\bar{\rho}}\nu_{sgs}\left(\tilde{S}_{ij} - \frac{1}{3}\delta_{ij}\tilde{S}_{kk}\right) \quad (8)$$

In compressible flows $\bar{\bar{\rho}}\nu_{sgs}$ in equation 8 is called turbulent viscosity μ_t. It is clear that equations 5 and 8 have the same structure and it is possible to write $\boldsymbol{\sigma} = \mu_{eff}[\nabla\mathbf{U} + (\nabla\mathbf{U})^{\mathrm{T}}] - \left(\frac{2}{3}\nabla \bullet \mathbf{U}\right)\mathbf{I}$ after LES filtering of equations 2 and 3 where μ_{eff} is called effective viscosity and calculated as $\mu_{eff} = \mu + \mu_t$. In order to add the effect of turbulence on the heat transfer and diffusion in the energy and species transport equation μ_t is also applied to calculate effective thermal conductivity and diffusion coefficients as $\lambda_{eff} = C_p\mu_{eff}/Pr_t$ and $D_{eff} = D_i + \mu_t/Sc_t$, respectively. Pr_t and Sc_t are turbulent *Prandtl* and turbulent *Schmidt* numbers , respectively and both had a value of 0.7 in the current study. In practice for LES modelling, computational fluid dynamics (CFD) codes use the governing equations with similar structures as presented in equations 1–4 with μ_{eff} replacing μ and **U** representing the resolved velocity field.

The wall-adapting local-eddy viscosity (WALE) SGS model (Nicoud and Ducros, 1999) was employed in the present study. This model is based on the square of the velocity gradient tensor and can take into account both shear and rotation. In comparison to the classical *Smagorinsky* model, the WALE model produces zero eddy viscosity in the case of a pure shear (may occur in free jets) that makes it capable of reproducing turbulent transitional processes more accurately through the growth of unstable modes (Nicoud and Ducros, 1999). In the WALE model μ_t is calculated as:

$$\mu_t = \rho\Delta^2 \frac{\left(S_{ij}^{d}\, S_{ij}^{d}\right)^{3/2}}{\left(\tilde{S}_{ij}\tilde{S}_{ij}\right)^{5/2} + \left(S_{ij}^{d}\, S_{ij}^{d}\right)^{5/4}} \quad (9)$$

where S_{ij}^{d} is the traceless symmetric part of the square of the velocity gradient tensor (Pope, 2000). Δ in equation 9 is the filter cut-off size and in the current study is obtained as $\Delta = C_w V^{1/3}$ in which C_w is a constant with a value of 0.544 and V denotes the volume of the local computational cell.

The governing equations were discretized spatially and temporally and consequently converted to a system of linearized algebraic equations by means of the finite volume (FV) method. The linearized governing equations were solved in a coupled approach (*i.e.* simultaneously) by using the Gauss-Seidel iterative technique in conjunction with an algebraic multigrid (AMG) method (Weiss *et al.*, 1999). The multigrid method is applied in order to accelerate the solution of the linearized system. Specifically, the concept is that long wavelength errors on the fine level appear as short wavelength errors on the coarser levels and hence can be more effectively damped out (Ferziger and Peric, 2002). In low *Mach* conditions and particularly within the incompressible limits (*Ma* < 0.3) the compressible governing equations become stiff. This is because, the variation of density becomes minute thus the pressure calculated using density and the equation of state is not associated entirely with the velocity field obtained from the conservation of momentum. Therefore, extra treatment is required to develop a computational framework for arbitrary *Mach* number

from the subsonic to the supersonic limits. In the current study preconditioning of the governing equations in conjunction with dual time-stepping (Weiss and Smith, 1995) is used in order to overcome the stiffness of the governing equations within low *Mach* number limits that may occur in locations within the volume of an under-expanded jet. Preconditioning of the governing equations destroys their time accuracy therefore for the second order implicit time marching approach used here it is required to perform some number of inner iterations to converge the solution for a given time step (dual time-stepping). The inner iterations is accomplished using implicit spatial integration that marches them using optimal pseudo-time steps ($\Delta\tau$) which are determined from the *Courant-Friedrichs-Lewy* (CFL) condition (Weiss *et al.*, 1999) as:

$$\Delta\tau = \min\left(\mathrm{CFL}\frac{|\mathbf{U}|}{\lambda_{max}}, \sigma\frac{(\Delta\mathbf{x})^2}{\nu}\right) \tag{10}$$

where λ_{max} is the maximum eigenvalue of the system of the linearized equations, σ is the *von Neumann* number ($\sigma \approx 1$). For the current study a value of CFL as low as 0.2 was employed initially which then increased gradually using a linear ramp.

A modified version of the advection upstream splitting method (AUSM$^+$-up) (Liou, 2006) was applied in order to express the inviscid fluxes. AUSM$^+$-up is accurate and robust in solving fluid flows containing any arbitrary range of velocity magnitudes and particularly high speed flows that contain extreme flow discontinuities such as shock waves (Liou, 2006). AUSM$^+$-up uses a separate splitting for the pressure terms of the governing equations and avoids an explicit artificial dissipation; the mass flux and pressure flux are calculated on the basis of local flow characteristics (including the speed of sound) to ensure precise information propagation inside the fluid for convective and acoustic processes (Liou, 2006). This reduces the numerical dissipation particularly in high velocity flows and consequently avoids wiggles at flow discontinuities such as shocks.

For the cases with hydrogen and methane injection in to air the molecular diffusivity was calculated using the *Chapman-Enskog* theory for gaseous diffusion coefficients as follows (Cussler, 2009):

$$D_i = \frac{1.86 \times 10^{-3} T^{3/2} \left(1/M_1 + 1/M_2\right)^{1/2}}{P_{atm}\sigma_{12}^2 \Omega} \tag{11}$$

where D_i is the coefficient of molecular diffusivity in cm^2/s, T is the absolute temperature in K, P_{atm} is the pressure in atm, M_1 and M_2 are the molecular weights. The quantities σ_{12} and Ω are molecular properties; σ_{12} is the collision diameter, given in Å, which is the arithmetic average of the two species (Cussler, 2009):

$$\sigma_{12} = 0.5(\sigma_1 + \sigma_2) \tag{12}$$

Values of σ_1 and σ_2 can be found in Cussler (2009). The values of the dimensionless quantity Ω depend on an integration of the interaction between the two species which can be described by the Lennard-Jones 12-6 potential and is usually of order unity (Hirschfelder, 1964).

2.2 Adaptive mesh refinement

Significantly fine spatial resolution is required in order to account for strong flow discontinuities (like shock waves) and turbulent mixing in under-expanded jets (Vuorinen *et al.*, 2013; Hamzehloo and Aleiferis, 2014b). Depending on the properties of the issuing gas and also operating conditions the use of a minimum grid size of at least *D*/20 is typically required, as widely practiced in the literature (White and Milton, 2008; Dauptain *et al.*, 2010; Velikorodny and Kudriakov, 2012; Vuorinen *et al.*, 2013; Hamzehloo and Aleiferis, 2014b). The common approach in modelling this type of flow is to apply a fixed refinement area with a varying cell size downstream of the nozzle exit (that would cover all or part of the jet volume) (Vuorinen *et al.*, 2013; Hamzehloo and Aleiferis, 2014b; Vuorinen *et al.*, 2014). For NPR values lower than about 6, and also for gasses with low diffusivity, this approach has been shown to be able to resolve completely the jet volume with reasonable cell count for quantifying the jet tip penetration (Vuorinen *et al.*, 2013; Vuorinen *et al.*, 2014). However, for high NPR values and/or highly diffusive gases such as hydrogen, this method would require a significant larger number of cells in order to resolve the entire jet volume accurately. A solution to this is to resolve with a fine grid only a portion of the jet core, as also practiced previously by the current authors (Hamzehloo and Aleiferis, 2014b; Hamzehloo and Aleiferis, 2014c). This practice has been found to offer the ability to resolve shock structures embedded in the jet core and also resolve a valuable portion of the mixing process in hydrogen and methane jets with NPR up to 10 within a reasonably practical cell count (~13.5 M cells). However, parts of the initial transient vortex rings of the under-expanded jets studied were located outside the refinement zone and consequently were not resolved in detail. Also, it was noticed that for NPR>20, a much larger refinement area was required, especially in the radial direction, in order to model accurately the *Mach* disk dimensions, core shock cells and turbulent mixing in the vicinity of the jet boundaries within a useful penetration length of the jet (~30*D*) (Hamzehloo and Aleiferis, 2014b; Hamzehloo and Aleiferis, 2014c).

In order to address the aforementioned issues of spatial resolution and to achieve a more accurate solution of under-expanded jets within still practical CPU times, a fully automatic AMR technique was developed by the user coding capability of STAR-CC+ based on Java programming. The AMR method was developed and tested on Cartesian grids but it can also be used for other types of cell types. The STAR-CCM+ version 9.02.007 used for the present study did not include a default AMR facility and the entire AMR procedure was developed purely by the current authors. The rest of this subsection is devoted to describing the implementation of the AMR technique.

Initially a simulation with AMR starts on a relatively coarse grid with only limited initial refinement zones created upfront. A refining parameter is then defined on the basis of a flow variable such as fuel mole fraction, density gradient, *etc.* The AMR process is triggered for a certain time interval depending on the growth rate of the flow. For the present study, AMR was based on the jet's scalar concentration (ρc) or mole fraction of fuel. The use of density gradient was avoided because this would result in significantly larger number of cells due to the propagation of spherical pressure waves ahead of the jet volume. Additionally, the

use of the density gradient alone may result in the formation of fairly coarse spatial resolution within the jet volume where the density gradient is not large enough to satisfy the predetermined refining threshold.

When the AMR is triggered with the mole fraction as refining parameter, all the cells with mole fraction equal or larger than the threshold are automatically detected. Then the computational grid is regenerated (by means of the trimmer facility of STAR-CCM+) using a table that contains the coordinates of those cells detected for refinement. The flow is automatically interpolated to the new cells using a distance-weighted, least-square interpolation (the solution data is mapped using a stencil of cells and faces on the original mesh). With this approach, the vertices/coordinates of the cells that are not refined (either because they were fine enough or were outside of the volume of interest) are kept intact. Transition from the finest to the coarsest grid resolution is designed through a 5-stage grid coarsening. This, in addition to a suitable AMR trigger timing, can ensure all the jet volume and some adjacent cell layers (see Figure 1) are being solved constantly within the finest uniform spatial resolution, typically considered to be $D/50$ for the jets studied in the current study. Therefore, some typical issues of AMR-LES with respect to treating the SGS kinetic energy by introducing a proper level of turbulent fluctuation to a newly refined cell and maintaining the conservation of kinetic energy through coarse-fine cell interfaces (Mitran, 2001; Pope, 2004; Pantano *et al.*, 2007; Antepara *et al.*, 2015) were avoided within the areas of interest, *i.e.* the jet and its adjoining volumes.

Figure 1 shows the performance of the AMR technique in modelling the initial stages of formation of an under-expanded nitrogen jet with NPR=8.5 (issued into a nitrogen-filled ambient). This test case will be discussed later in this paper and the focus here is only on the AMR procedure. The refinement parameter was the scalar concentration (ρc) with an AMR trigger threshold of ρc=0.01. As shown at t=13.5t_0 in **Figure 1**, the computational domain included a fixed initial refinement zone covering a distance of 0.8D downstream of the nozzle exit. This was applied in order to capture smoothly the initial pressure waves emitted from the nozzle exit. It can be seen that by using a suitable AMR interval (here this was set to 2 μs) and a five level grid refinement, the entire jet volume was solved continuously with a $D/50$ spatial resolution. This means that during each refinement interval, cells covering the jet volume remained intact while their surrounding cells were gradually refined. Comparison between t=22.5t_0 and t=24.0t_0 in **Figure 1** shows how AMR coarsened the spatial resolution of the grid with regards to the outline of the jet. It should be noted that in the current study the initial refinement zone was kept untouched during the simulations and AMR procedure. However, if required, any initial refinement zone(s) can be easily adjusted to the shape of the emerging jet.

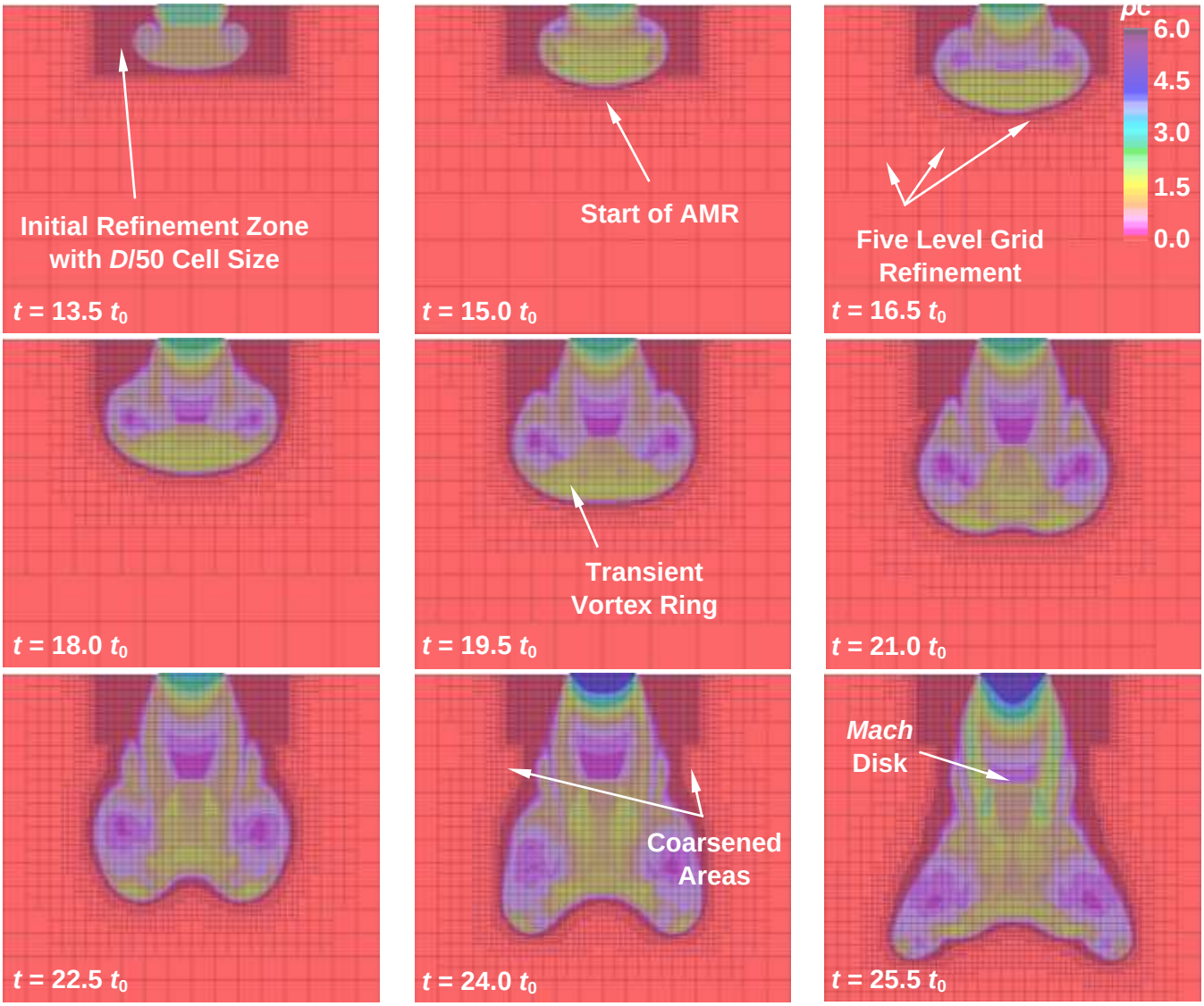

Figure 1. Adaptive mesh refinement used for modelling initial transient development of a highly under-expanded nitrogen jet with NPR=8.5.

The change in the total number of cells after the nozzle exit and a normalized jet tip penetration are both shown in **Figure 2** against a normalized time after the start of injection for the jet of **Figure 1**. In this figure $t \leq 12t_0$ is associated with the development of an initial subsonic jet that was also noticed in previous studies of under-expanded jets (Vuorinen *et al.*, 2013; Hamzehloo and Aleiferis, 2014b). Within the time frame of $12t_0 \leq t \leq 15t_0$ the nozzle exit became gradually choked with $Ma \approx 1.0$. At around $t \approx 15t_0$ the jet penetrated for almost $0.8D$ and reached the boundaries of the initial fixed refinement zone; the AMR was triggered after this time. At $t \approx 35t_0$ the increased rate of cell count overtook the penetration rate. This is because the cell count was affected by both tip penetration and volumetric growth of the jet. After the initial transient stages, the rate of the jet's penetration exhibited a decreasing trend while the total number of cells showed an almost constant increasing rate. According to **Figure 2** at almost $9D$ jet tip penetration (D=1.5mm) a total number of ~10 M cells were required in order to resolve the entire jet volume with $D/50$ spatial resolution. This indicates that although AMR could reduce the computational costs when modelling the initial development stages of under-expanded jets, it may result in significantly large cell count if applied throughout a much longer jet presentation process and/or for highly diffusive 'bulky' jets. Therefore, within the concept of

under-expanded jets, AMR should be treated as a technique for achieving a more accurate representation of the flow at specific stages rather than a tool aimed at reducing computational costs throughout the whole injection process.

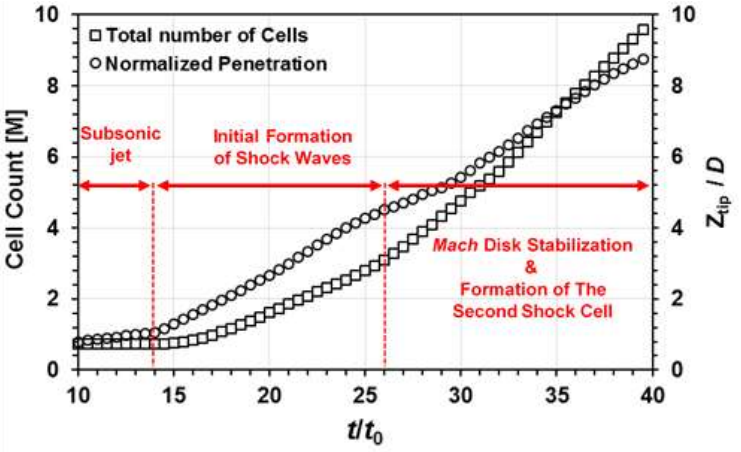

Figure 2. Variations of the total number of cells and the jet tip penetration (normalized with the nozzle exit diameter) versus time after start of injection normalized by t_0=2μs.

2.3 Simulation setup

In Hamzehloo and Aleiferis (2014b, 2014c), the ability of the current LES framework to model under-expanded jets without the AMR technique was discussed in detail and validated both quantitatively and qualitatively against the experimental data of Ruggles and Ekoto (2012) and other computational results (Vuorinen *et al.*, 2013; Yu *et al.*, 2013). In the present paper the AMR-based computational framework was validated against those previous studies but also using additional data in the literature (Edgington-Mitchell *et al.*, 2014; Vuorinen *et al.*, 2014). The remaining subsections describe the validation cases that were used.

2.3.1 Validation cases

Three test cases were prepared based on some recent experimental data of under-expanded jets available in the literature in order to validate the present AMR-LES framework. Some key details of these test cases are provided in **Table 1**. In all test cases, simulations of under-expanded jets were performed by considering systems consisted of a high pressure fuel tank and a low pressure air(nitrogen)-containing chamber that were linked by a converging nozzle. The configuration of these test cases are shown in **Figures 3–5**. The length of the high pressure tank was long enough so that the flow could be considered to be almost at rest at the inlet within the injection duration. This assumption which has also been used by other researchers (Dauptain *et al.*, 2010; Vourinen *et al.*, 2013; 2014) eliminated the need for applying any artificial perturbation for LES studies. It is worth mentioning that in under-expanded jets the dominant turbulent structures are created after the *Mach* reflection (*i.e.* the first shock cell) and the turbulence level at the nozzle exit do not play a significant role in main turbulent structures of the jet (Edgington-Mitchell *et al.*, 2014; André *et al.* , 2014). This is discussed further in the current paper (see **Figure 13**). In validation cases 1 and 3 (**Figures 3** and **5**) A stagnation pressure inlet condition was applied at the top boundary of the high-pressure tank in order to maintain the injection pressure, while the side and the bottom boundaries of the low pressure chamber were

set to pressure outlet. However, in test case 2 (**Figure 4**) the configuration is entirely wall-bounded similarly to the configuration reported in the literature (Vourinen *et al.*, 2013; 2014). Following practices in the literature (Dauptain *et al.*, 2010; Vuorinen *et al.*, 2013; Vuorinen *et al.*, 2014), the wall of the converging nozzle and the high pressure reservoir were set to adiabatic slip in order to avoid formation of any artificial boundary layer. Computational grids consisting of cubic elements were created by using the trimmer facility of STAR-CCM+. This produced cells with identical size in all dimensions and resulted in a grid without cell stretching which typically provides enhanced numerical accuracy and avoids singularity issues linked to polar grids.

Table 1. Test cases of under-expanded jets investigated in this study.

Case	Experimental data	Geometry	Gas, ambient	D [mm]	NPR	P_∞ [bar]	T_∞ [K]	T_o [K]	Diffusivity	AMR threshold	AMR interval [μs]
Validation 1	Ruggles and Ekoto (2012)	Figure 3	H_2, air	1.5	10	0.9837	296	295.4	D_i=7.94×10^{-5} m^2/s	X=0.01	0.1
Validation 2	Vuorinen *et al.* (2013, 2014)	Figure 4	N_2, N_2	1.4	8.5	1.0	293	293	Sc=0.7	ρc=0.01	2.0
Validation 3	Edgington-Mitchell *et al.* (2014)	Figure 5	Air, air	15	4.2	1.0140	297	293	Sc=0.7	ρc=0.01	10
Elevated P_∞	N/A	Figure 3	H_2, air	1.5	10	9.837	296	295.4	D_i=7.94×10^{-6} m^2/s	X=0.01	0.1
Elevated P_∞, T_∞	N/A	Figure 3	H_2, air	1.5	10	9.837	600	295.4	D_i=2.29×10^{-5} m^2/s	X=0.01	0.1
Elevated P_∞, T_∞	N/A	Figure 3	CH_4, air	1.5	10	9.837	600	295.4	D_i=6.1×10^{-6} m^2/s	X=0.01	0.1

For the all simulations a fixed refinement area was implemented inside the computational domain. For the test case with configuration shown in **Figure 3** the initial refinement area was stretched just ~2.5D downstream of the nozzle exit. In total about 3.5 M calls filled initially the computational domain. This was ~4 times smaller than when a fixed grid without AMR was used to model a similar jet (Hamzehloo and Aleiferis, 2014b). The simulation started from rest conditions where it was assumed that hydrogen (methane) occupied the entire high pressure reservoir and a tiny part of the converging nozzle volume up to ~1.4D upstream the nozzle exit. Air occupied the low pressure ambient and the remaining of the in-nozzle volume. The nominal integral time scale of an under-expanded gaseous jet issued from a circular nozzle can be defined as t_0=D/2U$_e$ (Vuorinen *et al.*, 2013). Assuming choked conditions at the nozzle exit (Ma=1), t_0 was calculated to be ~6.2×10^{-7} s for the hydrogen jet. A time-step in the range of Δt=1×10^{-9}–5×10^{-9} was used with lower values at the early stages of the simulation for modelling the in-nozzle transient flow. Molecular diffusivity was considered according to the *Chapman-Enskog* theory with values tabulated in **Table 1**. In the current study the dynamic viscosity was calculated using *Sutherland's* law with *Sutherland's* constant (C_s), reference value (μ_s) and reference temperature (T_s) given in **Table 2**.

Table 2. Sutherland's constants for different gases.

Gas	C_s [K]	μ_s [Pa.s]	T_s [K]
H_2	72.0	8.76×10^{-6}	293.9
CH_4	197.8	1.2×10^{-5}	273.15
N_2	111.0	1.781×10^{-5}	300.55
Air	120	1.827×10^{-5}	291.15

For the test case shown in **Figure 5** the use of no-slip wall condition was inevitable due to the relatively large diameter of the nozzle. The initial grid had a conical refinement area that occupied a region from 2*D* upstream of the nozzle exit to 0.5*D* downstream of the nozzle exit. The rest of the nozzle volume was filled with a resolution of *D*/25 which then stretched to a maximum cell size of 1.0 mm through a 5-level grid expansion. 25 prism layers with 0.15 mm thickness and a stretching rate of 1.5 were applied in order to resolve the viscous boundary layer for the converging nozzle and the bottom wall of the high pressure tank. This guaranteed a y^+ lower than unity which is required for accurate LES work with no-slip walls. The nominal integral time step of the flow was calculated to be $t_0 \approx 2.4\times10^{-5}$ s (U_e=310 m/s), therefore, a time step of $\Delta t = 1\times10^{-6}$ s was selected.

2.3.2 Elevated ambient pressure and temperature cases

The configuration used for validation case 1 was also used to investigate the effect of elevating the ambient pressure and temperature on the sonic and mixing characteristics of under-expanded hydrogen jets with respect to application in hydrogen-fuelled IC engines (Hamzehloo and Aleiferis, 2014a). These cases have been included in **Table 1**. The simulation with T_∞=296 K and P_∞=98.37 kPa represents an 'early injection' strategy occurring just after intake valve closure in the compression stroke of a naturally aspirated direct-injection hydrogen engine and is typical for homogeneous mixture formation. The simulation with T_∞=600 K and P_∞=983.7 kPa represents a 'late injection' strategy occurring close to ignition timing at the end of the compression stroke that is typical for stratified engine operation. Then a simulation with T_∞=296 K and P_∞=983.7 kPa was also conducted. This case was not of immediate reference to a typical in-cylinder operating condition but was used in order to decouple the effects of pressure and temperature. Nevertheless, it may be seen as a test case that could provide insights towards heavily boosted engines. Similarly to validation case 1, the nominal integral time scale of those simulations was ~6.2×10^{-7} s; however, a time step of $\Delta t = 1\times10^{-9}$ s was used throughout the simulations in order to account for the existence of relatively higher incoming momentum. Furthermore, direct comparison was conducted between hydrogen and methane jets with NPR=10 issued into air with P_∞=983.7 kPa and T_∞=600 K. Although the nominal integral time step for the methane jet was fairly larger than that of hydrogen jet (due to the considerably lower speed of sound in methane, (Hamzehloo and Aleiferis, 2014b), a similar time step ($\Delta t = 1\times10^{-9}$ s) to that of the aforementioned hydrogen jet was also used for this methane jet.

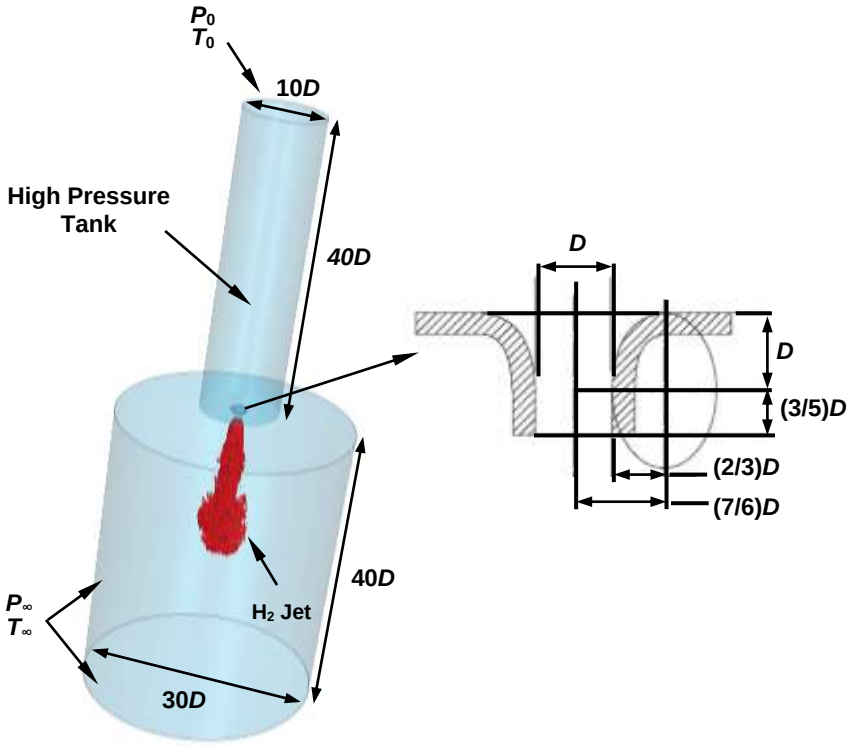

Figure 3. Domain configuration and dimensions with nozzle profile based on Ruggles and Ekoto (2012).

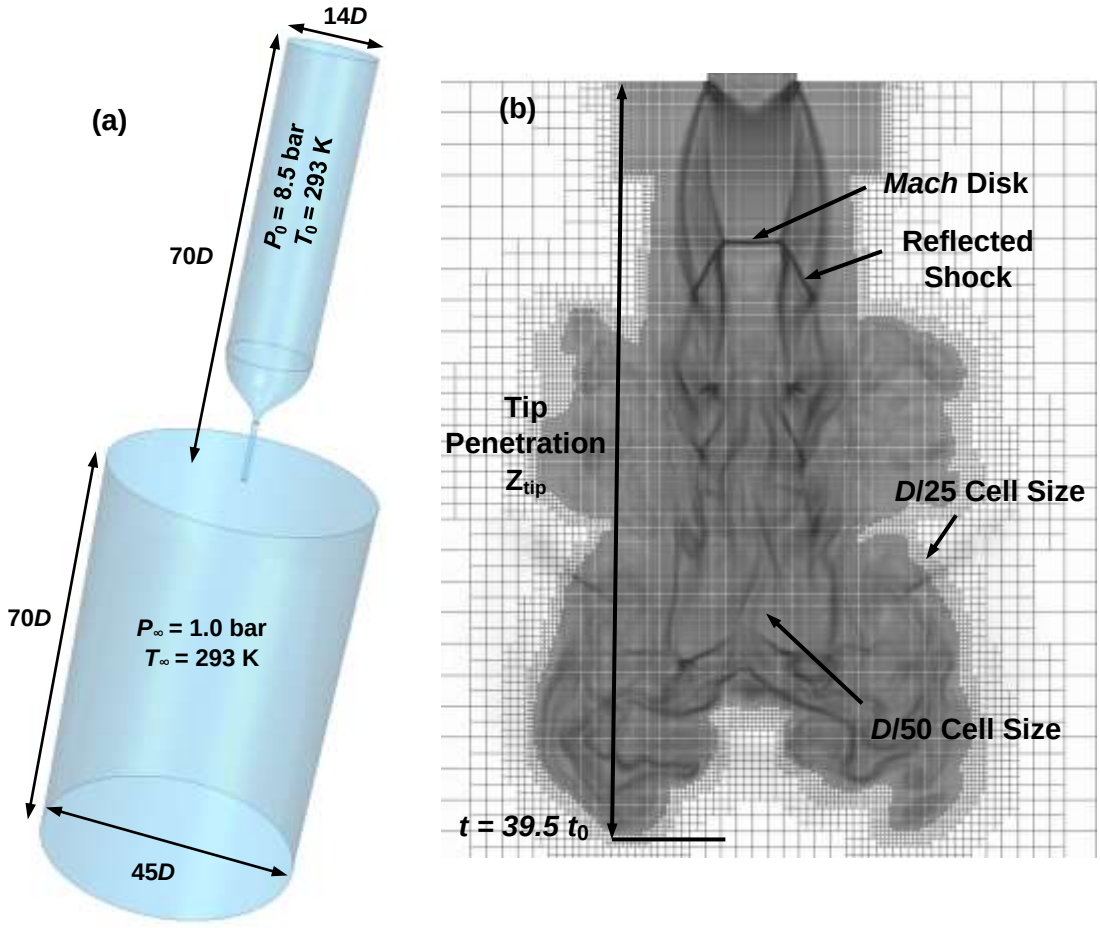

Figure 4. Left: Domain configuration and dimensions; geometry based on Vourinen *et al.* (2013). Right: Zoomed view of the AMR refined area.

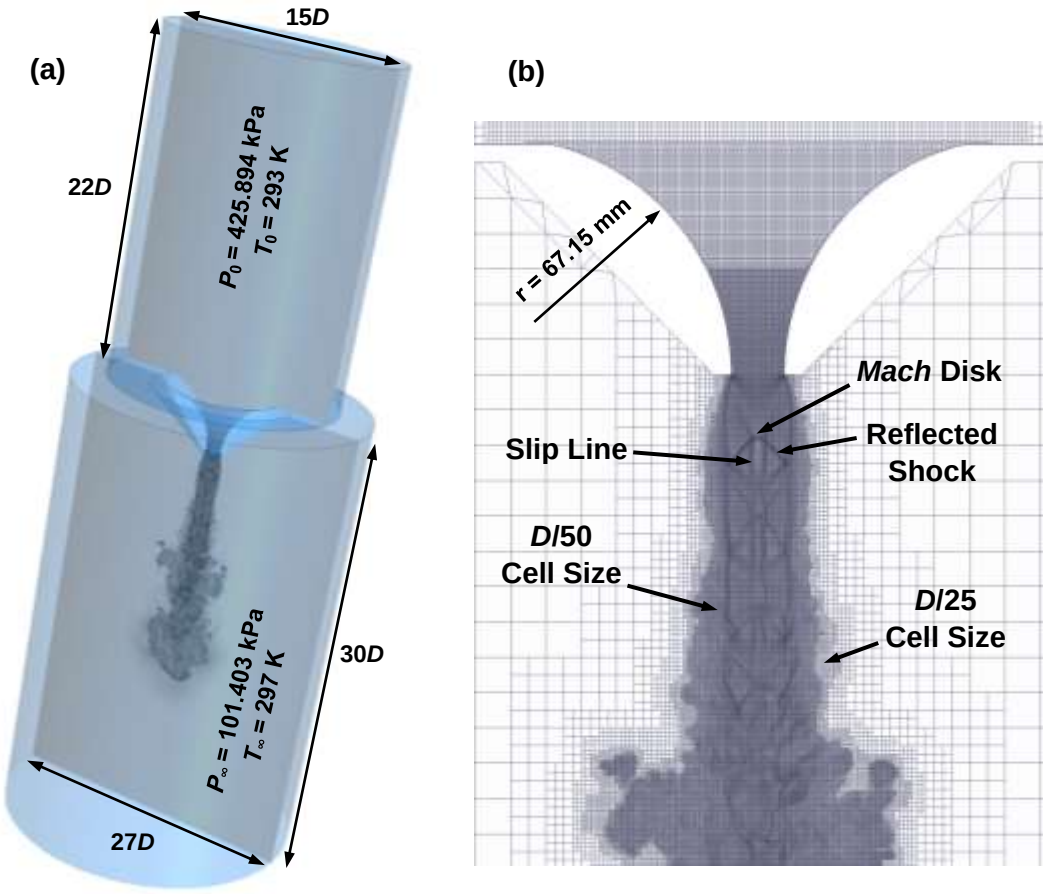

Figure 5. Left: Domain configuration and dimensions; geometry based on Edgington-Mitchell *et al.* (2014). Right: Zoomed view of the AMR refined area with some important features of an under-expanded jet.

3. Results and discussion

3.1 Model validation

3.1.1 Validation case 1

Figure 6 compares instantaneous fields of $\log_{10}(|\nabla\rho|)$ for the hydrogen jet under study with AMR and the hydrogen jet investigated in the study of Hamzehloo and Aleiferis (2014b) with a fixed refinement zone. It has been observed in earlier studies (Golub, 1994) that the *Mach* disk of an under-expanded jet exhibits an initial fluctuation around its final semi-steady dimensions. Previously in Hamzehloo and Aleiferis (2014b) it was noticed that for the hydrogen jet of **Figure 6** without AMR the near-nozzle shock structure and *Mach* disk dimensions reached semi-steady conditions in t=40–50 μs. **Figure 6** shows that at t=35 μs the *Mach* disk dimensions of the hydrogen jet with AMR were almost identical to those of jets modelled without AMR at $t\geq$40 μs. An overall good agreement was observed between the *Mach* disk dimensions, H_{disk}=3.08 mm and W_{disk}=1.34 mm, and the near-nozzle shock structure between the hydrogen jets of the two studies, in accordance with the experimental investigation of Ruggles and Ekoto (2012).

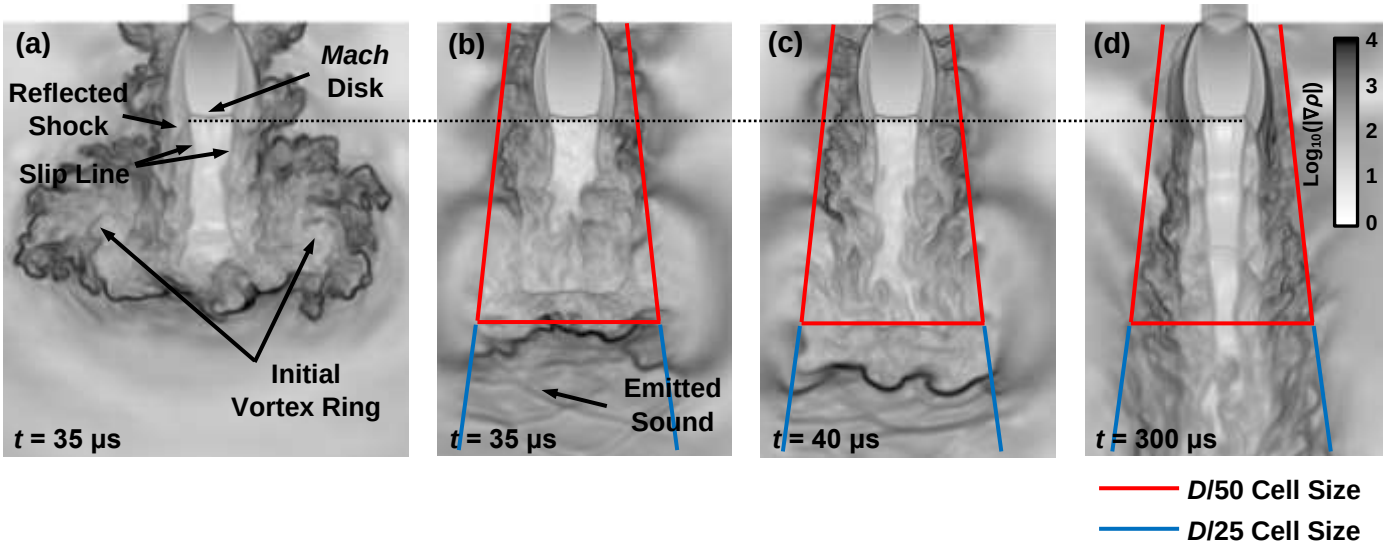

Figure 6. Near-nozzle shock structure in under-expanded hydrogen jets with NPR=10 injected in to an ambient air with P_∞≈1 bar with AMR (a) in the present study and without AMR (b–d) in previous study (Hamzehloo and Aleiferis, 2014b).

Direct comparison between the tip penetration of the hydrogen jets with and without AMR is illustrated in the left graph of **Figure 7**. It was found that until *t*≈20 μs both jets exhibited almost identical penetration length. However, after this time the jet modelled by means of AMR displayed around 8% lower tip penetration compared to the jet simulated with fixed refinement. Also, at *t*=35 μs the latter jet showed around 3% higher centreline penetration in comparison to the former jet (see (a) and (b) snapshots of **Figure 6**). The relatively smaller penetration of the jet with AMR is attributed to its better resolved jet tip vortices *i.e.* its initial transient vortex ring. The earlier investigation of Hamzehloo and Aleiferis (2014b) revealed that for this hydrogen jet at around *t*=20 μs (when penetration differences start to show in **Figure 7**), tip vortices started penetrating radially beyond the fixed refinement region and consequently were resolved with marginal quality. A better resolved vortex ring with AMR is more dominant and introduces fairly stronger radial expansion; hence by considering almost identical hydrogen mass flow rate at the nozzle exit for both cases with and without AMR, a shorter axial penetration (both tip and centreline) is expected for the jet modelled with AMR. Comparison between the snapshots (a) and (b) of **Figure 6** clearly shows the enhancement achieved in resolving tip vortices by means of AMR.

As explained in Ouellette and Hill (2000), Vuorinen *et al.* (2013) and Hamzehloo and Aleiferis, (2014b), for under-expanded jets the jet tip penetration Z_{tip} can be scaled with the ratio of the upstream stagnation density to the ambient density ρ_0/ρ_∞ as $Z_{tip}/(\rho_0/\rho_\infty)^{1/4} \sim t/{t_0}^{1/2}$. The right graph of **Figure 7** shows that the penetration curves of hydrogen and methane AMR collapsed on top of each other comparably to the previous observations of Vuorinen *et al.* (2013) and Hamzehloo and Aleiferis (2014b). The discrepancy of the penetration of the jet without AMR after $t/{t_0}^{1/2} > 6$ in this figure originated from the aforementioned resolution inaccuracy of the jet tip vortices.

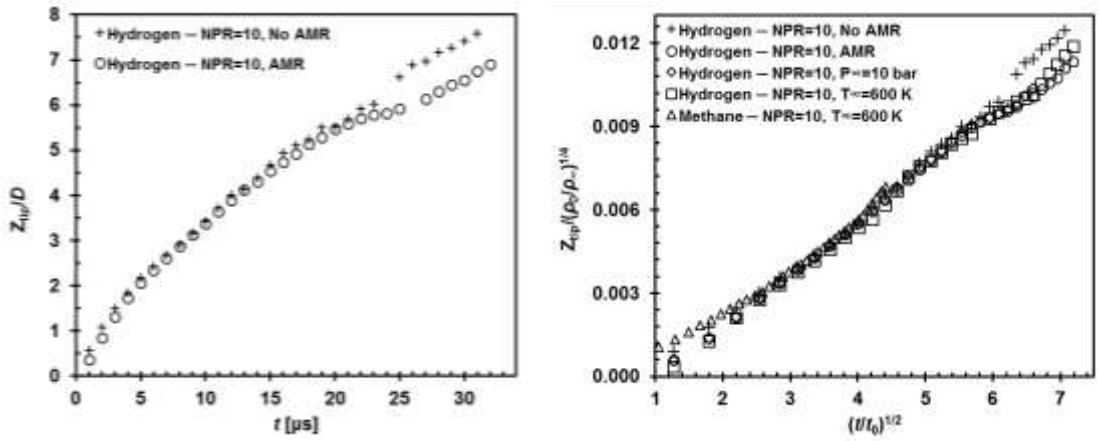

Figure 7. Left: Normalized jet tip penetration with the nozzle diameter (D=1.5 mm) of hydrogen jets with NPR=10 and P_∞≈1 bar modelled with and without AMR. Right: Scaled jet tip penetration of hydrogen and methane jets studied (with and without AMR) versus a normalized time.

3.1.2 Validation case 2

Figure 8 compares the average near-nozzle density field of an under-expanded nitrogen jet with NPR=8.5 modelled by LES in Vuorinen *et al.* (2014) and LES with AMR of the present study. The figure has been scaled in the same way to that presented in Vuorinen *et al.* (2014). Moreover, **Figure 9** shows a direct comparison between the current work and the average concentration field (ρc) of the same nitrogen jet produced experimentally and computationally in Vuorinen *et al.* (2013); snapshots (a)–(d). Snapshot (e) of **Figure 9** shows the average field of $\log_{10}(|\nabla\rho|)$ with similar legend to those of **Figure 6**. The *Mach* disk dimensions were found to be H_{disk}= 2.57 mm and W_{disk}=0.97 mm and these are in agreement with values reported by Vuorinen *et al.* (2013, 2014). Specifically, the current study predicted ~1% and 3% smaller *Mach* disk dimensions compared to those reported in Vuorinen *et al.* (2013) and Vuorinen *et al.* (2014), respectively. This is attributed to the fact that, unlike the present study and Vuorinen *et al.* (2013), a temperature dependent specific heat capacity at constant pressure (C_p) was used in Vuorinen *et al.* (2014). The angle of the reflected shock at the triple point was found to be α≈28.5°, which is comparable to observations reported in Vuorinen *et al.* (2013).

Snapshots (c) and (d) of **Figure 9** show the average ρc field plotted with different legend upper value for better visualisation. Direct comparison between the regions highlighted by dotted white ovals in snapshots (a) and (d) of **Figure 9** reveals close similarity with regards to the topology of the outer shear layer between the current LES study and the experimental visualisation of Vuorinen *et al.* (2013).

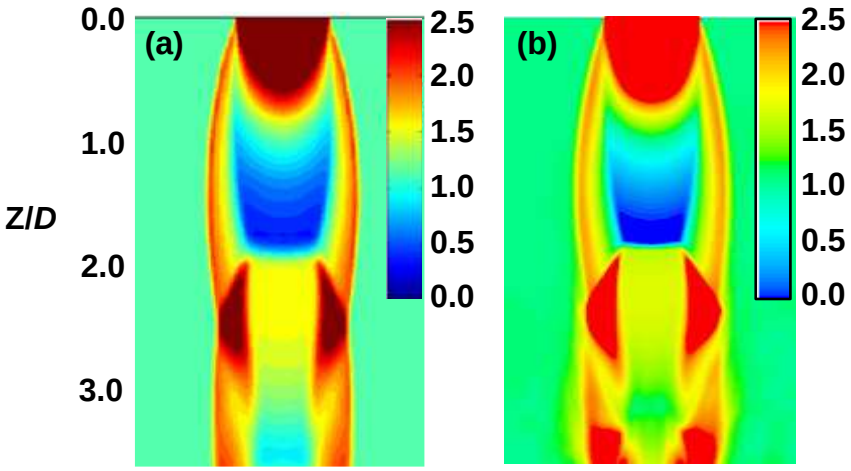

Figure 8. Averaged near-nozzle density field of an under-expanded nitrogen jet with NPR=8.5. (a): LES of Vuorinen *et al.* (2014). (b): LES of the present study with AMR.

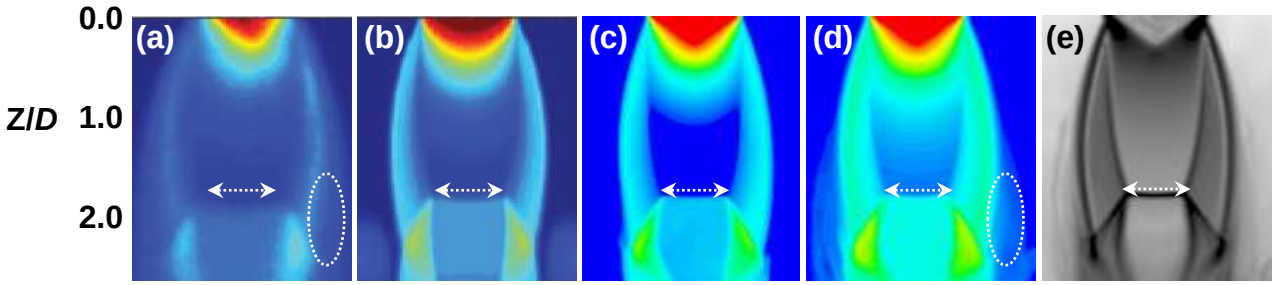

Figure 9. (a)–(d): Comparison between average concentration (ρc) of an under-expanded nitrogen jet with NPR=8.5 produced (a): experimentally by Vuorinen *et al.* (2013), (b): computationally by Vuorinen *et al.* (2013) and (c)–(d): computationally in the present study with different legends. (e): Averaged field of $\log_{10}(|\nabla\rho|)$ produced by the present study.

Similarly to **Figure 7**, **Figure 10** compares the scaled penetration length of the nitrogen jet of the current study with that reported by Vuorinen *et al.* (2013). In agreement with the literature (Ouellette and Hill, 2000; Vuorinen *et al.*, 2013; Hamzehloo and Aleiferis, 2014b), it is clear that the scaled penetration curves collapsed on almost a single line. This confirms that in addition to the sonic characteristics, the current computational framework was also able to reproduce accurately the penetration length.

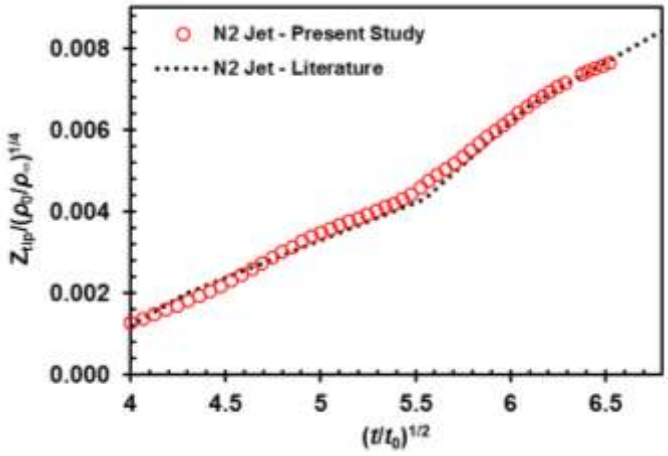

Figure 10. Scaled jet tip penetration of a nitrogen jet with NPR=8.5 versus a normalized time. Comparison between the present LES study with LES of Vuorinen *et al.* (2013).

3.1.3 Validation case 3

Figure 11 is based on an under-expanded air jet with NPR=4.2 and compares predictions of the current LES study with experimental data reported by Edgington-Mitchell *et al.* (2014). The current LES framework reproduced the height and width of the *Mach disk* ~6% and ~17% smaller compared to the measurements obtained from Schlieren visualisation. Initially this difference may be explained due to the necessary simplifications applied (see **Figure 5**) when creating the computational model of the quite complex experimental apparatus shown in Edgington-Mitchell *et al.* (2014). As seen previously (Donaldson and Snedeker, 1971; Vuorinen *et al.*, 2013), the dimensions of the *Mach* disk and particularly its width are a function of NPR. During the experiment, upstream pressure and consequently NPR might experience some level of oscillations which could affect the *Mach* disk dimensions noticeably. Another contributing factor can be the level of turbulence at the nozzle exit. In fact as also reported in Vuorinen *et al.* (2013) and Yu *et al.* (2013), the level of turbulence at the nozzle exit in an experimental test case can be significantly higher than that of its computational model. It has been reported (Golub, 1994) that *Mach* disk dimensions of under-expanded jets exhibit slight fluctuations even after reaching a semi-steady condition. Higher turbulence level at the nozzle exit may intensify these fluctuations and result in larger *Mach* disk dimensions experimentally in comparison to what predicted numerically. Similarly to what was discussed for validation case 2, the last contributing factor to the difference between LES and experiment in *Mach* disk dimensions can be attributed to the lack of temperature dependency of C_p in the simulations. Since the difference between the computational and experimental *Mach* disk dimensions in the current case is slightly higher than those discussed in previous test cases, the authors believe that the reason for this difference is a combination of the aforementioned factors. The previous test cases used simpler experimental apparatuses with almost 10 times smaller nozzle diameters than that of test case 3. Therefore, effects of NPR fluctuations and nozzle exit turbulence may be less significant in the first two test cases.

In general, as presented in snapshots (a)–(f) of **Figure 11**, the current LES study was able to reproduce the near nozzle shock structures comparably to those observed in the experiments. The reflected shock angle with the nozzle centreline was predicted ~3° larger than that of the experiments with also slightly narrower distance between the slip lines (the length of the red arrows in snapshots (a), (d) and (e) of **Figure 11** are identical). This was attributed to the smaller *Mach* disk width of the numerical prediction. Similarly to the Schlieren images, the current LES study predicted the expansion and shrinkage of the width of the subsonic core (*i.e.* distance between the slip lines) just after the *Mach* reflection (discussed comprehensively in Edgington-Mitchell *et al.*, 2014). A combination of the shock structures and turbulent behaviours of the under-expanded air jet can be seen in snapshot (g) of **Figure 11** which is based on instantaneous contours of $\log_{10}(|\nabla\rho|)$ at t=1.5 ms. The general bulk shape of the jet with its turbulent behaviour was captured computationally in agreement with earlier observations of this kind of jet (Donaldson and Snedeker, 1971; Dauptain *et al.*, 2010; Vuorinen *et al.*, 2013, Vuorinen *et al.*, 2014). After the *Mach* reflection, several shock cells formed and after a certain distance from the nozzle exit viscous forces became dominant and consequently the shock cells disappeared (mixing of inner and outer shear layers started) and the jet became highly turbulent and exhibited intense mixing with the ambient medium, particularly at its boundary.

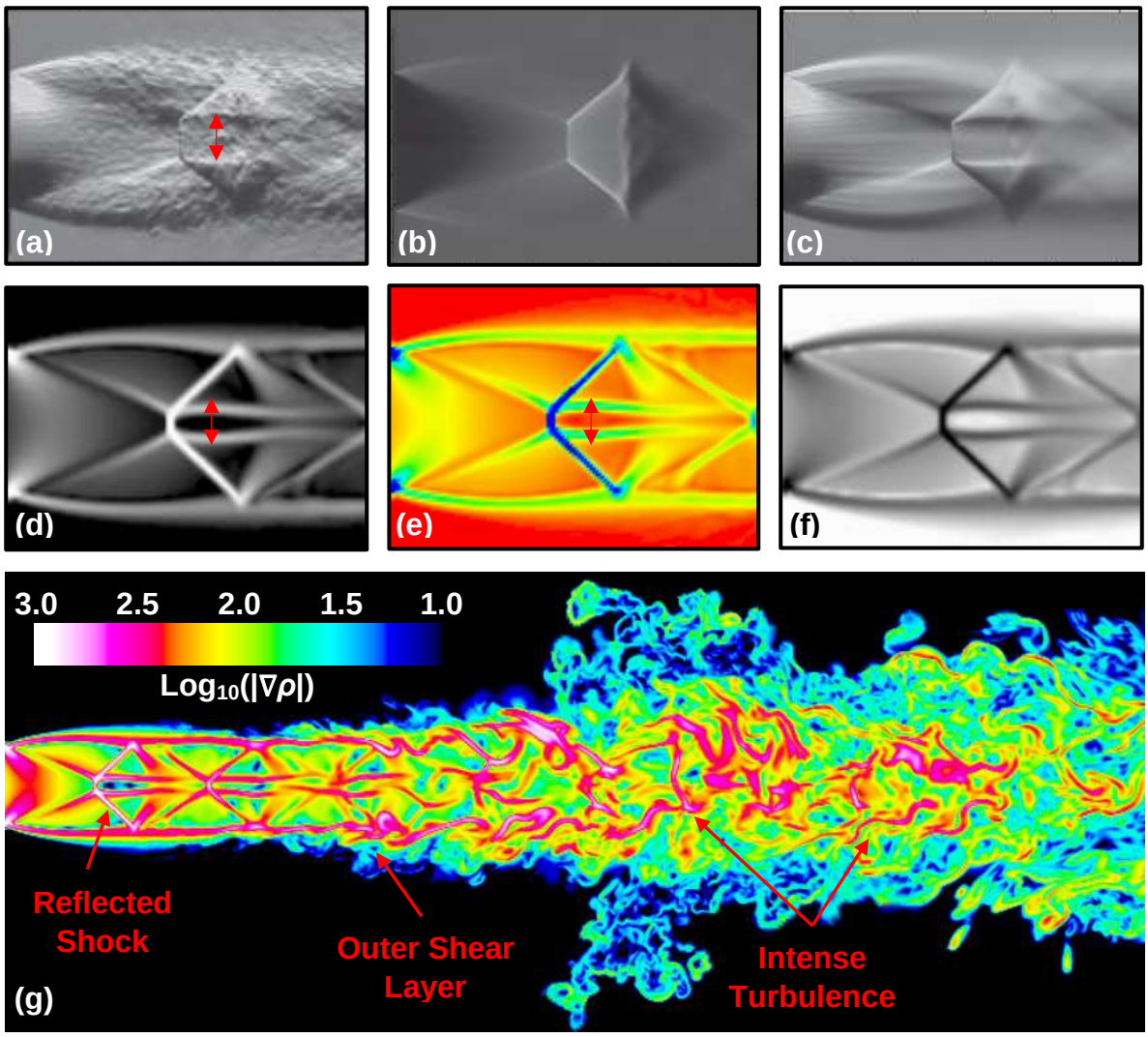

Figure 11. Near nozzle shock structure and turbulent behaviour of the under-expanded air jet with NPR=4.2 issued from a circular nozzle with *D*=15 mm. (a): Instantaneous Schlieren image of dρ/dX (Edgington-Mitchell *et al.*, 2014). (b, c): Averaged Schlieren images of dρ/dZ and dρ/dX, respectively (8000 samples, Edgington-Mitchell *et al.*, 2014). (d, e): Instantaneous contours of the magnitude of the density gradient ($|\nabla\rho|$) with different legend colours by LES. (f): Averaged contours of $\log_{10}(|\nabla\rho|)$ by LES (200 samples). (g) Instantaneous contours of $\log_{10}(|\nabla\rho|)$ at *t*= 1.5 ms by LES. (For interpretation of the references to colour in this figure legend, the reader is referred to the web version of this article.)

A direct comparison between contours of mean in-plane velocity components (up to Z=4*D* downstream of the nozzle exit) produced by the current LES and planar PIV measurements of (Edgington-Mitchell *et al.*, 2014) is presented in **Figure 12**. The averaging of experimental data was conducted over 8000 samples while for LES the averaging was conducted over 200 samples. This was due to the fact that by the time the near-nozzle flow reached a semi-steady condition in the LES simulation, AMR had produced ~21 M cells and further running of the simulation was not really feasible within reasonable CPU timescales. In **Figure 12** the black line indicates an approximation of $w/U_e \approx 1$ in both experimental and computational visualisations (U_e is the velocity at the nozzle exit). Very good agreement was observed with the experimental data in some classical characteristics of under-expanded jets such as initial formation of the outer shear layer at the nozzle exit (can be clearly seen in the w/U_e snapshots of **Figure 12**), *Mach* reflection, oblique shocks at the triple

point and inner shear layer. Slight differences are attributed to the noticeably different number of samples used to evaluate the average values for each case.

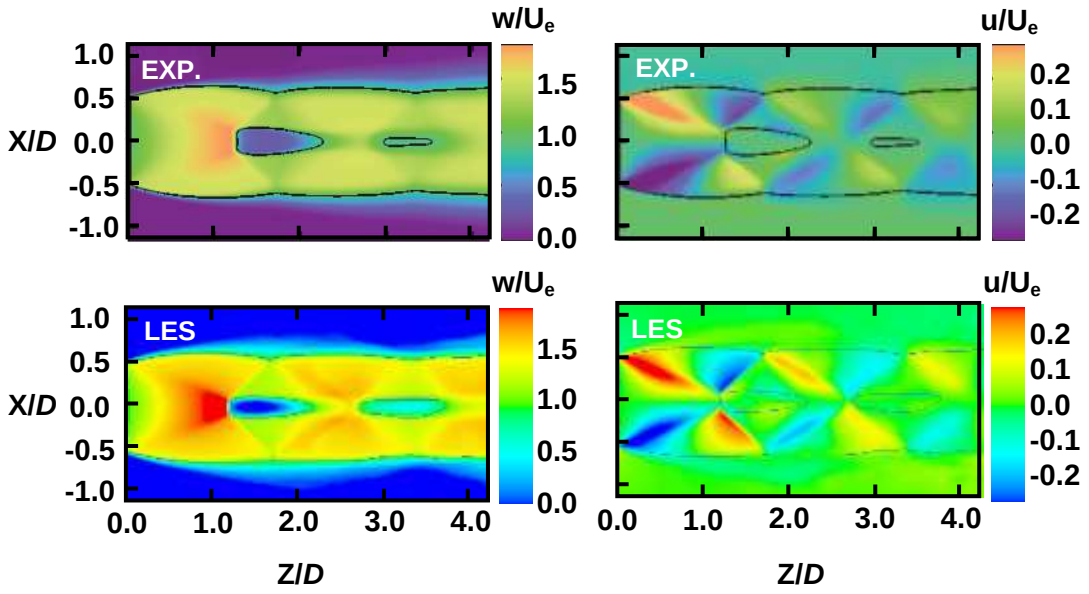

Figure 12. Contours of mean in-plane velocity components normalized by the nozzle exit velocity U_e≈310m/s (the under-expanded air jet with NPR=4.2). Top row: Experimental data of Edgington-Mitchell *et al.* (2014) averaged over 8000 samples. Bottom row: The current LES representation averaged over 200 samples. The black line indicates an approximation of w/U_e≈1 in both experiments and LES.

Centreline profiles of first- and second-order statistics of the velocity are plotted in **Figure 13** for both LES and PIV. With respect to the mean axial velocity, the LES-derived curve follows relatively closely the trend of the experimental curve. However, compared to measurements, the maxima and minima of the LES curve are ~2% higher and ~85% lower, respectively (w/U_e=1.89, 0.037 for LES compared to w/U_e =1.85, 0.28 for PIV). Extremely low values of velocity just after the *Mach* disk of under-expanded jets have also been reported by other computational studies in the literature (Velikorodny and Kudriakov, 2012; Owston *et al.*, 2009). This noticeable difference between experiments and simulations is attributed to the existence of a strong flow discontinuity due to the *Mach* reflection. If very high spatial resolution is used, simulations may be able to resolve the flow behaviour in the vicinity of the *Mach* disk more accurately. A similar behaviour between LES and PIV comparison has been reported by Dauptain *et al.* (2010). The effect of the spatial resolution in the prediction of the *Mach* discontinuity in under-expanded jets has been discussed in Owston *et al.* (2009) where it was shown that a relatively coarse grid may not be able to capture precisely the near-nozzle velocity profile of under-expanded jets.

After the *Mach* reflection at Z=10*D* downstream of the nozzle exit, LES predicted six peaks *i.e.* six shock cells, compared to five peaks quantified by PIV (see **Figure 13**). This was due to the aforesaid slight difference in the *Mach* disk height between computations and measurements which produced a small phase lag between the curves of velocity in **Figure 13**. This means that the sixth peak of the experimental data would probably be located after Z=10*D* and was not captured. As discussed by Pack (1950), the spacing of the shock cells after the *Mach* reflection in an under-expanded jet should be almost identical. **Figure 13** shows that, despite the slight frequency difference, the spacing between the velocity peaks (shock cell

spacing) in both computational and experimental curves remained constant and was ~22 mm for both curves. This was comparable to classical observations (Donaldson and Snedeker, 1971) and theoretical studies (Pack, 1950) of this kind of flow. It is worth mentioning that similarly to the experimental observations of Edgington-Mitchell *et al.* (2014) the current LES did not reproduce a second normal shock after the *Mach* reflection. With respect to velocity fluctuations, it is clear from **Figure 13** that both the axial and transverse fluctuations experienced modulation by the embedded shock structures. At the jet core, similarly to experimental observations, LES predicted more modulation for the transverse fluctuation than the axial one, mainly due to the relatively lower effects of the shear layers within this region. Although the bulk trend of the fluctuation graphs of **Figure 13** is similar between computations and experiments, some differences are observed. For Z/*D*<1.2, *i.e.* upstream of the *Mach* disk, LES predicted noticeably lower axial and transverse velocity fluctuations (w'/U_e ranging from 2×10^{-4} to 10^{-3} and u'/U_e ranging from 8×10^{-6} to 1.2×10^{-4}) compared to those of PIV (w'/U_e ranging from 1.2×10^{-2} to 3×10^{-2} and u'/U_e ranging from 7.5×10^{-3} to 9×10^{-3}). This is attributed to the fact that no artificial perturbation was applied in the current LES study. The turbulent characteristics of under-expanded jets are greatly amplified by the *Mach* reflection and resilient shear layers downstream of the *Mach* disk (Inman *et al.*, 2008). Different averaging samples between LES and experiments (200 and 8000, respectively) may also contribute to the discrepancy between the velocity fluctuation graphs of **Figure 13** particularly for Z>4*D* downstream of the nozzle exit where the jet structure exhibited strong turbulent behaviour (see snapshot (g) of **Figure 11**). However, as seen in **Figure 13** and particularly for w'/U_e, good agreement was observed between LES and PIV for 1.2<Z/D<4.5. Within this range the u'/U_e graph of **Figure 13** shows larger difference in magnitude between LES and PIV when compared to the w'/U_e graph, but still a similar overall trend exists. This can be due to the aforementioned difference between the turbulence intensity upstream of the *Mach* disk. Such intensity difference can have a greater effect on the transverse velocity fluctuation than on the axial mainly due to the stronger effect of the flow discontinuity and shear layers on the axial velocity profile.

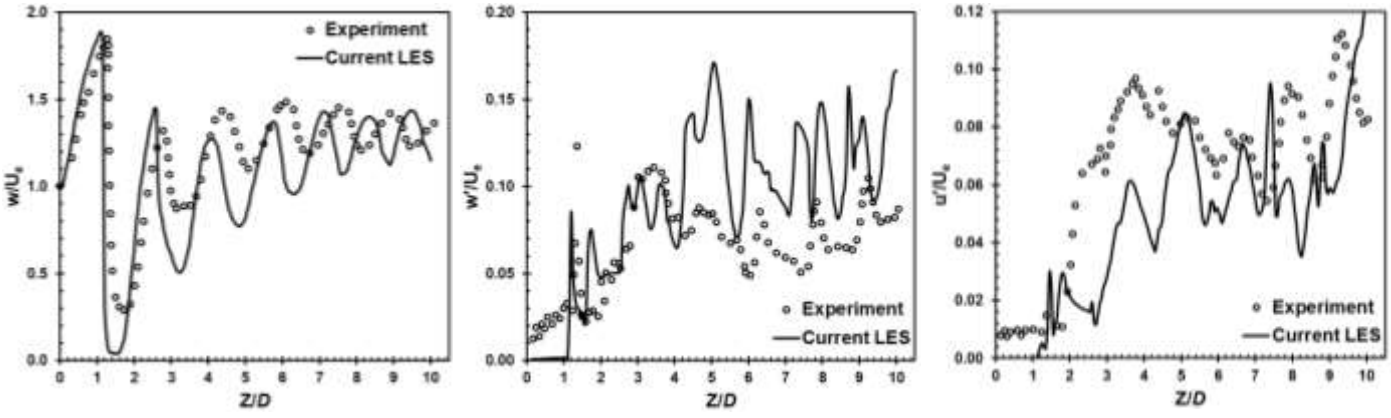

Figure 13. Axial profiles of mean and fluctuating velocity quantities taken along nozzle centreline in the under-expanded air jet with NPR=4.2. Comparison between the current LES study and PIV data reported in Edgington-Mitchell *et al.* (2014).

3.2 Penetration and volumetric growth

3.2.1 Various ambient thermodynamic conditions

The jet tip penetration, volumetric growth and number of cells created by AMR within the low pressure ambient are plotted in **Figure 14** versus time for hydrogen. It was found that hydrogen jets with NPR=10 and T_∞=296 K but with different ambient pressures of $P_\infty \approx$ 1 bar and 10 bar followed almost identical trends. This may be due to the fact that the sonic characteristics of under-expanded jets are mainly a function of NPR. Therefore, with identical NPR a fairly similar velocity distribution forms downstream of the nozzle exit which results in comparable radial and axial penetrations.

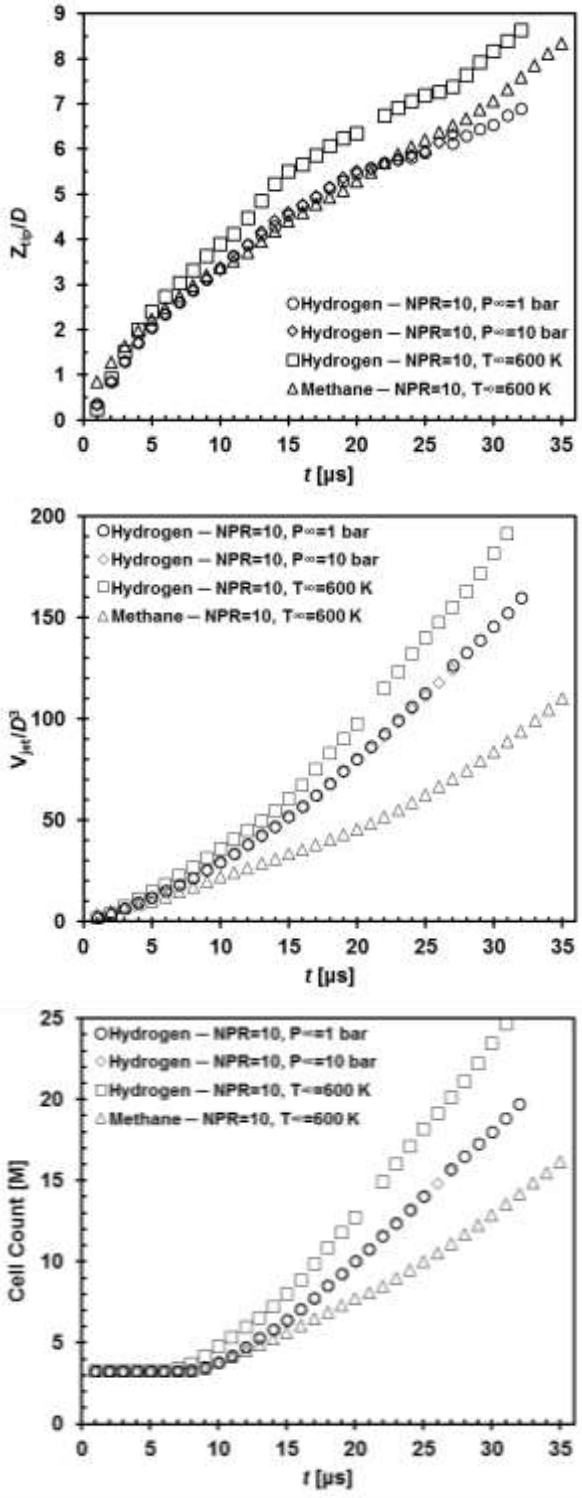

Figure 14. Variations of normalized tip penetrations, normalized volume and cell count of under-expanded hydrogen and methane jets investigated in the current study.

Increasing the ambient temperature at P_∞=10 bar from T_∞=296 K to T_∞=600 K resulted in increased jet tip penetration and volumetric growth, and consequently increased AMR cell count. Specifically, at t=30 μs the hydrogen jet with T_∞=600 K exhibited ~21% longer penetration and ~30% larger volumetric growth in comparison to the jet with identical NPR and P_∞ issued into ambient air with T_∞=296 K. This was attributed to the lower density of the ambient at the higher temperature (ρ_∞≈5.7 and 11.6 kg/m^3 for 296 and 600 K, respectively). Similar to the present LES study, the experimental visualisations of Petersen and Ghandhi, (2006) and Rogers *et al.* (2015) also reported a reduction in the axial penetration of under-expanded hydrogen jets as a result of increased ambient density. About 9% difference in the effect of ambient temperature on the axial and radial penetration was attributed to the diffusivity difference under different ambient temperatures. At P_∞=10 bar, the diffusivity of hydrogen in an air at T_∞=600 K is ~188% higher than that at T_∞=296 K. Due to the presence of quite high axial velocity magnitude (in excess of 2000 m/s) the effect of diffusivity may not be as influential on the axial jet penetration as is on the radial penetration and consequently on the jet's volumetric growth.

Due to the relatively higher penetration and volumetric growth of the hydrogen jet with T_∞=600 K, the AMR produced at t=30 μs ~35% more cells (~21 M) for this jet compared to the hydrogen jet with T_∞=296 K (~15.5 M cells). Direct comparison between the cell count graphs of **Figure 14** and **Figure 2** shows that at ~6D penetration length, a hydrogen jet with NPR=10 requires ~180% more cells compared to a nitrogen jet with NPR=8.5 (~20 and 6.7 M cells, respectively). Despite the small difference in their NPR values, the significant cell count difference between these jets originates from the existence of stronger radial expansion of the transient vortex ring and higher diffusivity of hydrogen (characteristics of transient vortex rings in under-expanded hydrogen jets are discussed later in the current paper).

3.2.2 Hydrogen vs. methane

Figure 14 also illustrates a direct comparison between the under-expanded jets of hydrogen and methane at NPR=10 for P_∞=10 bar and T_∞=600 K. Hydrogen exhibited significantly higher penetration and volumetric growth compared to methane. Specifically, at t=30 μs, hydrogen showed ~16% and ~117% higher penetration and volumetric growth, respectively compared to methane jet (Z_{tip}≈10.62 mm and V_{jet}≈283 mm^3). This is in agreement with previous experimental observations (Petersen and Ghandhi, 2006) and also with the earlier study of Hamzehloo and Aleiferis (2014b) on under-expanded hydrogen and methane jets with NPR=8.5, P_∞=1 bar and T_∞=296 K. From **Figure 14** it is also observed that for t≥25 μs, the difference between the penetration rate of hydrogen and methane remained almost constant, ~0.35 mm/μs, while the rate of volumetric jet growth of hydrogen exhibited a fairly faster increase than that of methane (~32 mm^3/μs and 17 mm^3/μs for hydrogen and methane jets, respectively). This resulted in AMR's creation of more cells for the hydrogen jet; at t=30 μs ~23.5 M cells were required to resolve the hydrogen jet entirely with D/50 spatial resolution while with the same criteria only ~13 M cells were required for the methane jet. The difference in the volumetric growth rate is attributed to the significant differences in nozzle exit velocity and consequently radial expansion of the jet, as well as to the diffusivity differences between hydrogen and methane. In general, in comparison to all hydrogen jets studied (with and without elevated ambient),

methane showed noticeably lower volumetric growth. However, as shown in **Figure 14**, after $t \approx 24$ μs, the methane jet showed longer penetration compared to the hydrogen jets with identical NPR when injected into ambient air at T_∞=296 K. This is attributed purely to the difference in ambient density and associated reduction in the resistance of the ambient medium as discussed earlier.

3.2.3 Volumetric growth scaling

Using LES and scaling for the jet tip penetration (as suggested by Ouellette and Hill, 2000, and shown earlier in **Figures 7** and **10**), Vuorinen *et al.* (2013) proposed a specific scaling parameter for the volumetric growth of under-expanded jets as $V_{jet}/(\rho_0/\rho_\infty)^{3/4} \sim (t/t_0)^{3/2}$. The volumetric growth of the under-expanded jets examined in the current paper is plotted in the left graph of **Figure 15** using the aforementioned volumetric scaling correlation. It is seen that scaling created curves with almost linear growth rate. However, only the curves associated with hydrogen jets at T_∞=296 K collapsed on a single line. It was found that by introducing a multiplication coefficient β into the scaling parameter of Vuorinen *et al.* (2013), with values of 1.35 and 3 for hydrogen and methane, respectively, the curves of elevated ambient pressure and temperature collapsed onto the line of hydrogen jets with T_∞=296 K, as shown in the right graph of **Figure 15** (the value of β at the reference case of T_∞=296 K is obviously equal to unity for both P_∞=1 bar and 10 bar). The under-expanded nitrogen jets studied by Vuorinen *et al.* (2013) had similar molecular diffusivity, ratio of specific heats (*i.e.* sonic characteristics) and also resistance of the ambient medium (*i.e.* ambient density) (since they were injected into a cold nitrogen ambient with molecular diffusivity values calculated based on a fixed *Schmidt* number of 0.7). The under-expanded hydrogen and methane jets studied here had noticeably different values for the aforementioned quantities, therefore, their volumetric growth could not be scaled simply by the correlation suggested by Vuorinen *et al.* (2013). The β coefficient proposed here accounts for the possible effects due to differences in the diffusivity, sonic characteristics, and ambient density and as shown in **Figure 15** it is necessary to use it when comparing jets with quite dissimilar values of the mentioned quantities.

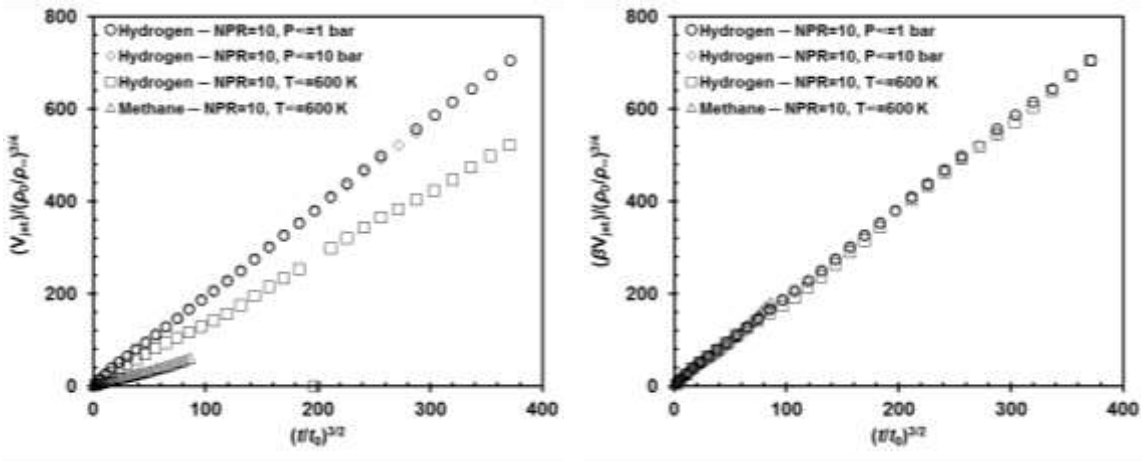

Figure 15. Normalized scaling parameter of the volumetric growth of under-expanded jets without (left) and with (right) the effect of parameter β.

3.3 Transient vortex ring

3.3.1 Hydrogen vs. methane

The initial stages of transient penetration of both hydrogen and methane injected into ambient with T_∞=600 K for a period of the first 30 μs after the start of injection are presented in **Figure 16** by means of mole fraction contours on a vertical symmetry plane of the nozzle. Due to the higher speed of sound in hydrogen compared to that of methane, the former jet entered the domain ~3 μs earlier. Therefore, methane's contours are included from t=6 μs in **Figure 16**.

A concave tip profile can be seen for both hydrogen and methane jets just after their initial penetration stage, t=4 μs and 6 μs, respectively. A similar concave behaviour has been noticed in previous experimental and computational studies that examined moderately under-expanded helium jets (Thangadurai and Das, 2010; Zhang, 2014). This was attributed to the existence of an embedded shock and the difference in velocities of the flow processed by this shock at different radii from the nozzle symmetry axis. This shock has a slightly convex profile which around the nozzle centreline performs almost similarly to a normal shock. While moving radially, the angle of inclination of the flow decreases and it can be treated as an inclined, *i.e.* not normal, shock (Hornung, 1986). This means that by moving away from the nozzle's symmetry axis, the flow velocity after the embedded shock increased and formed a shear layer which consequently created the concave profile at the tip of the jet. The flow at small radii after this embedded shock accelerated very quickly, reaching supersonic conditions and forming a fully convex tip profile in both hydrogen and methane jets after t≈6 and 8 μs, respectively.

Initial complete rolling-up of the tip occurs at t=5 μs for hydrogen, *i.e.* around t=3 μs faster than that of the methane jet. For the hydrogen jet, complete tip vortex was formed by t=8 μs and merged rapidly with strong shear layers (inner and outer) of the jet, becoming imperceptible at t=12–15 μs. By formation of the shock cells after the *Mach* reflection and formation of counter-rotating vortices close to the jet tip around its centreline (the latter due to *Biot-Savart* induction and vortex sheet roll-up, Thangadurai and Das, 2010; Zhang, 2014) seen clearly for both hydrogen and methane in the t=15 μs snapshots of **Figure 16**, the secondary vortex ring was formed at t≈25 μs. This then diffused to the surrounding ambient (and/or merged with the main jet stream) after vortex disconnection (or 'pinch-off') (Gharib *et al.*, 1998) from the trailing jet (t≥30 μs). In contrast, for methane, the initial vortex ring existed up to t=25–28 μs and then merged with the shear layers by a broadly similar mechanism to that described for hydrogen and formed a secondary set of vortices, as shown in the t=30 μs snapshot of **Figure 16**. Significant differences between the two gases in **Figure 16**, especially in terms of penetration, volumetric growth and shear layer development, were attributed to differences in their sonic characteristics and also the higher diffusivity of hydrogen; more details can be found in Hamzehloo and Aleiferis (2014b) as the main jet features were similar at low ambient temperature as well.

Further investigation on the basis of velocity vectors can shed more light onto the complex formation mechanism of the jets' vortex ring and annular shear layers. Snapshots of velocity vectors, hydrogen mass fraction and density gradients were overlapped using various degrees of opacity to provide a more complete image of the interactions involved. These are presented in **Figures 17** and **18**. The initial stages of the tip roll-up of the hydrogen jet are presented in **Figure 17**. At t=4 μs it is evident that the flow separated from the

edge of the embedded shock, satisfying the *Kutta* condition (Thangadurai and Das, 2010). The directionality of the arrows at t=6 μs demonstrates the tendency of the vortex to expand radially. This contributes to the outward expansion of the jet and formation of the outer shear layer before the location of the *Mach* disk (as also observed in Hamzehloo and Aleiferis, 2014b). Sudden expansion and *Prandtl-Meyer* expansion fans at the nozzle lip also contributed to the high radial velocity and associated behaviour of the jet. At t=6 μs, the tip vortices had significant contribution to the mechanism of entrainment of ambient air into the main stream of the fuel jet. Based on the flow behaviour seen in **Figure 17** it is now possible to explain the difference between the preliminary vortex rings of methane's and hydrogen's jets observed in **Figure 16**. Due to the significantly lower velocity of the under-expanded jet of methane than that hydrogen, relatively weaker separation occurred at the edge of the embedded shock in the former jet. Therefore, the vortex ring of methane required more time for a complete recirculation which then resulted in axial translation of the vortex core to significantly larger distances downstream of the nozzle exit compared to the maximum axial movement of the initial vortex core of the respective hydrogen jet.

In order to provide further fundamental understanding of the formation mechanism of the secondary vortex ring in the hydrogen jet, the t=15 μs snapshot of **Figure 16** was recreated in **Figure 18** using the overlapping features of **Figure 17**. A rather complex flow, consisting of several counter-rotating vortices with different intensities, was observed. It was found that the supersonic flow processed by the reflected shock at the triple point (within the slip region) was the main cause of the jet open-up and formation of the secondary vortex core. The complex configuration of the embedded shocks, followed by the formation of the shock cells (after the *Mach* disk) and also the existence of strong shear layers are believed to be the key contributors to this flow structure. The presence of many counter rotating vortices in **Figure 18** is believed to be due to *Kelvin-Helmholtz* type of instabilities (due to the high levels of shear) which promote transition of the vortex ring from laminar to turbulent (Thangadurai and Das, 2010).

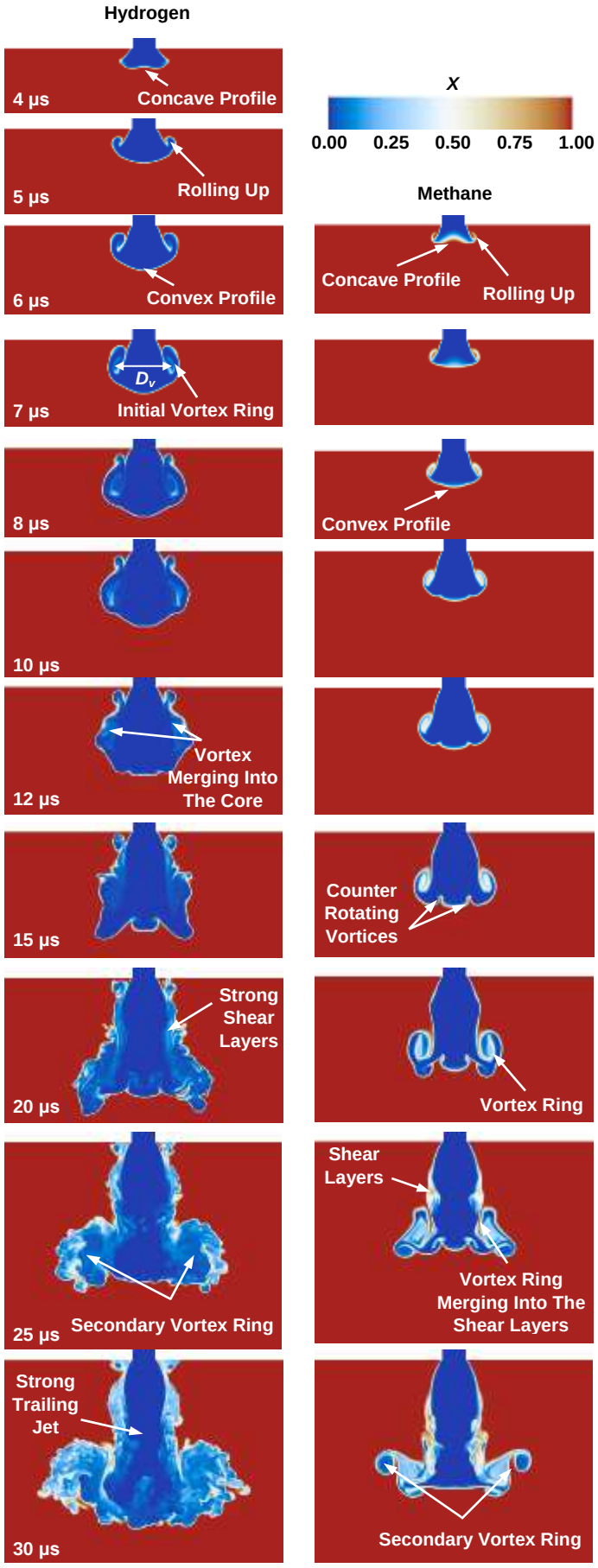

Figure 16. Transient development of under-expanded hydrogen and methane jets; formation and evolution of the vortex ring (P_∞=10 bar T_∞=600 K).

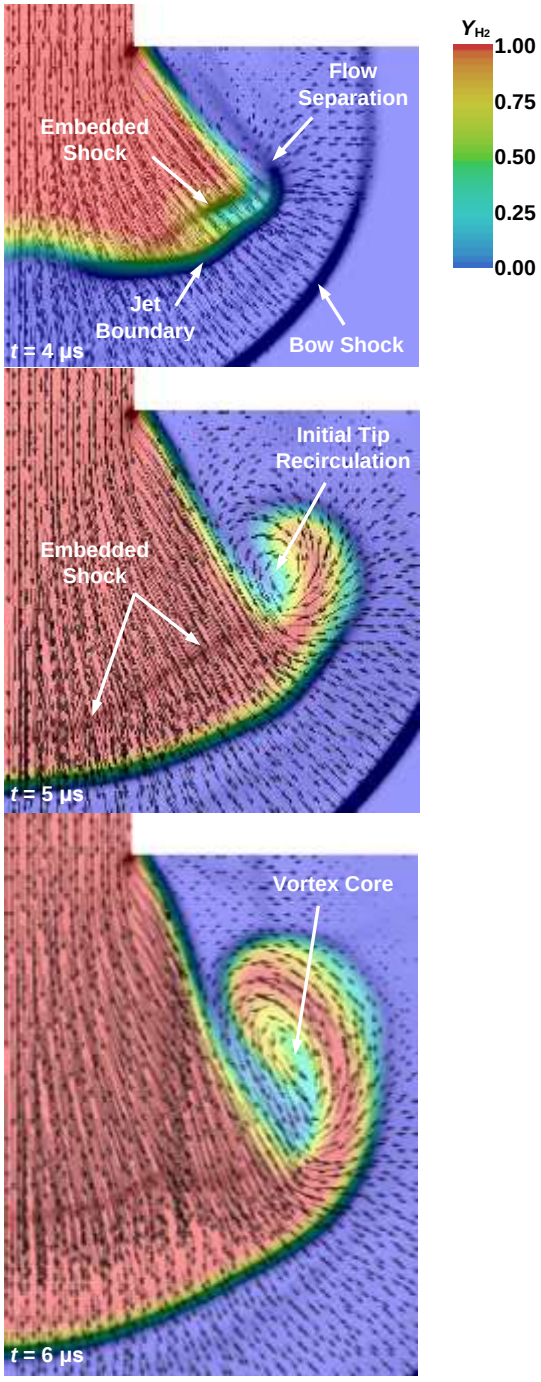

Figure 17. Flow separation at the edge of the embedded shock structure, rolling-up of the jet tip and formation of the initial tip recirculation in the hydrogen jet with P_∞=10 bar T_∞=600 K. The figure was made of overlapping velocity vectors, contours of hydrogen mass fraction and contours of the magnitude of the density gradient.

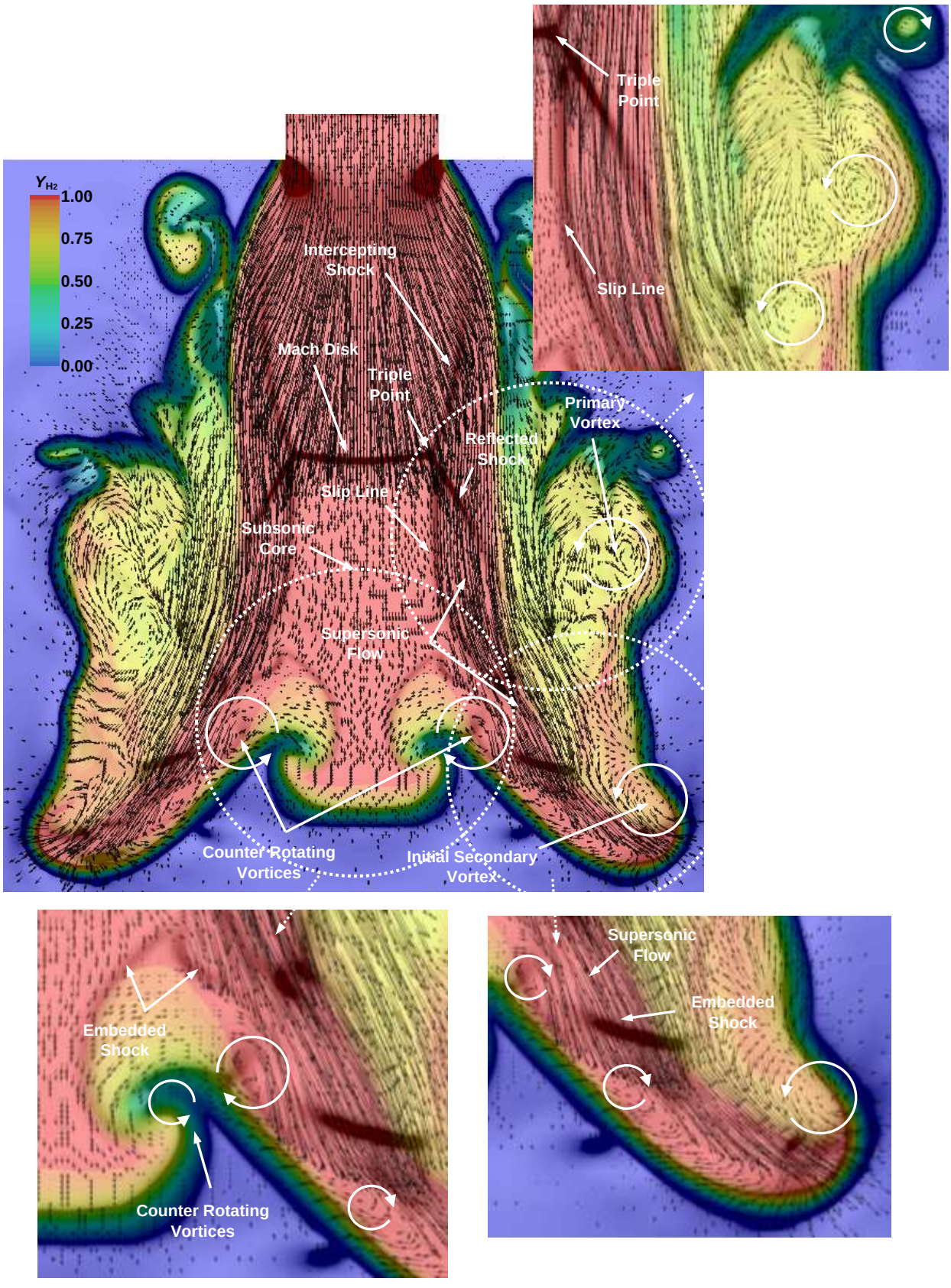

Figure 18. Flow characteristics of the under-expanded hydrogen jet with P_∞=10 bar and T_∞=600 K at t=15 μs. This picture is made of overlapping snapshots of the same parameters used in Figure 19.

3.3.2 Three-dimensional structures

The strongly three-dimensional vortical structures of under-expanded jets may not be fully distinguishable by visualisations in 2D like those of **Figure 16**. Therefore, 3D visualisations of the transient development of the vortex ring in the methane and hydrogen jets are presented in **Figures 19 and 20**. These are based on the iso-surface of methane's or hydrogen's mole fraction with a threshold value of X=0.01. It is clear that the vortex ring ahead of the trailing jets exhibited a poloidal-toroidal structure. For the methane jet up to t=20 μs a smooth vortex ring existed which in the 2D snapshots of **Figure 16** was identified on the basis of the symmetrical shape of the jet. **Figure 19** shows that within the time frame of t=20–25 μs the smooth vortex ring exhibited cellular structures through a gradual transient process. The formation of the transient vortex ring was the sign of the start of the fuel-ambient mixing process. For hydrogen the turbulent vortex ring formed significantly earlier in comparison to methane, at t=12 μs, and this was associated with the faster formation of the shear layers seen in **Figure 16**.

The iso-surfaces of **Figure 19** clearly show stationary vortical structures (streamwise and spanwise vortices Krothapalli *et al.*, 1998) close to the nozzle exit. These vortical structures exhibited helical motion around the circumference of the jet downstream of the *Mach* reflection and consequently were found to promote mixing at the jet boundary when studied later in their development process in Hamzehloo and Aleiferis (2016b). The cellular structure of the vortex ring in the *iso*-surface snapshots of **Figure 19** for t=29 μs demonstrated the existence of turbulent mixing between methane gas and ambient air.

A vortex ring normally disconnects from its training jet, in a pinch-off process, when the vorticity in the shear layer of the trailing jet ceases to flow into the vortex ring (Gharib *et al.*, 1998). The pinch-off process occurs for different reasons in different types of vortex rings and in the case of under-expanded jets it may be attributed to the high supersonic velocity of the fully developed shear layers. After formation of the supersonic slip region (and also shock cells), the velocity of the trailing jet becomes greater than that of the core of the vortex ring. At this point, pinch-off starts and the vortex ring reduces gradually in intensity, diffuses into the ambient gas and/or merges with the main stream of the gas jet. On the basis of **Figures 16** and **19** it can be concluded that the pinch-off process started at $t\approx$30 μs for methane. However, for hydrogen, as highlighted earlier, the pinch-off process occurred at a later time in the jet's development, and for its secondary vortex ring, hence a distinctly different behaviour occurred.

It was also found that the secondary vortex ring of the hydrogen jet was considerably stronger and wider than its initial predecessor. This can be attributed to the fact that the secondary ring was formed by the high velocity shear layers, as further elaborated on later in the paper. On the other hand, the secondary vortex ring of methane's jet was formed due to the pinch-off of its long-lasting preliminary vortex ring, therefore, it was relatively weaker and may not contribute significantly to the mixing process, or at least not to the same degree that it contributed for the hydrogen jet. These differences in the characteristics of the vortex rings between hydrogen and methane contributed to the formation of a relatively bulkier jet with wider cone angle for hydrogen compared to methane at fixed NPR, as can also be seen in the earlier simulated data of Hamzehloo and Aleiferis (2014b) and also in the experimental observations of Rogers *et al.* (2015).

Direct comparison between the vortex rings of methane's and hydrogen's jets (**Figures 19** and **20**) revealed that hydrogen's vortex ring started exhibiting a cellular structure much earlier than the methane jet, around t=15 μs. This shows that the fuel-air mixing started relatively earlier for hydrogen which at this stage is attributed to the higher diffusivity of hydrogen compared to that of methane. The cellular vortex ring structure of the hydrogen jet presented in **Figure 20** is in a very good agreement with the experimental visualisations of under-expand hydrogen jets provided by Petersen and Ghandhi (2006) and Rogers *et al.* (2015). These cellular structures of 3D visualisations are in fact the tiny counter-rotating vortices similar to those shown in **Figure 18**.

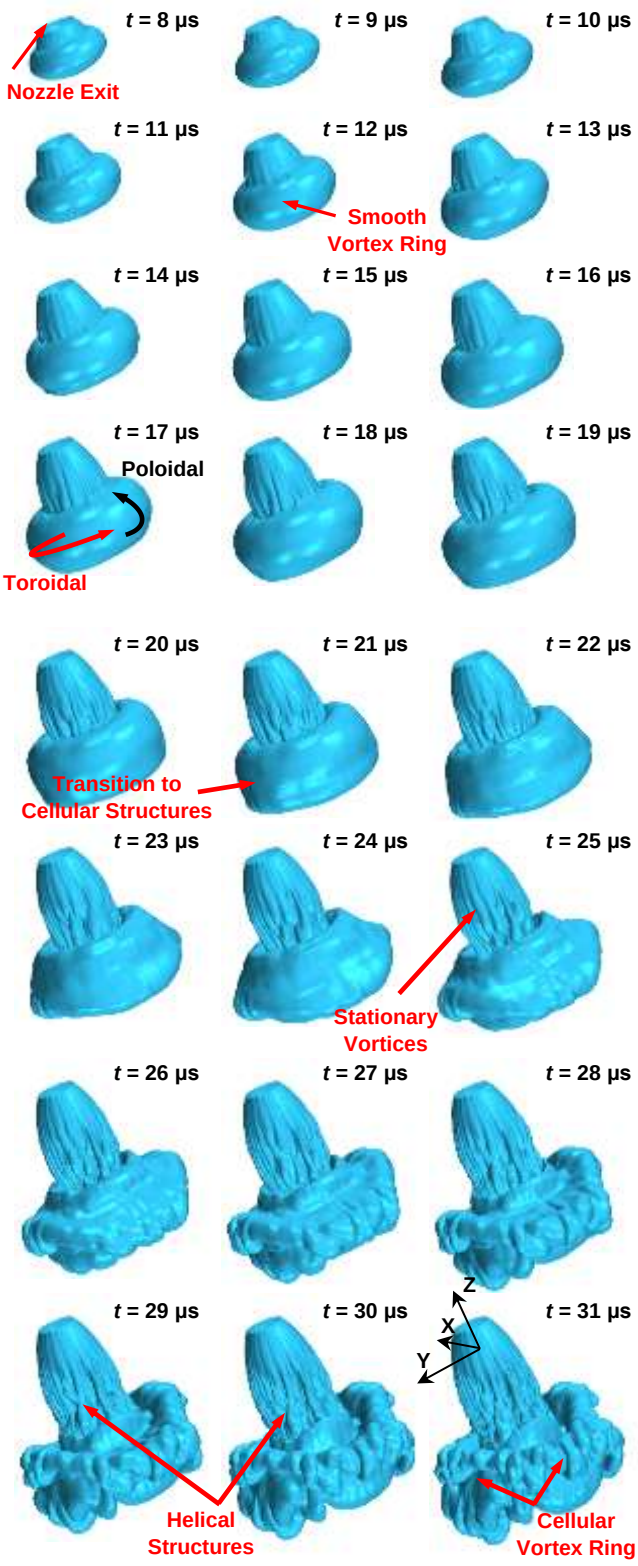

Figure 19. Three-dimensional visualisation of the preliminary vortex ring in the under-expanded methane jet with P_∞=10 bar T_∞=600 K.

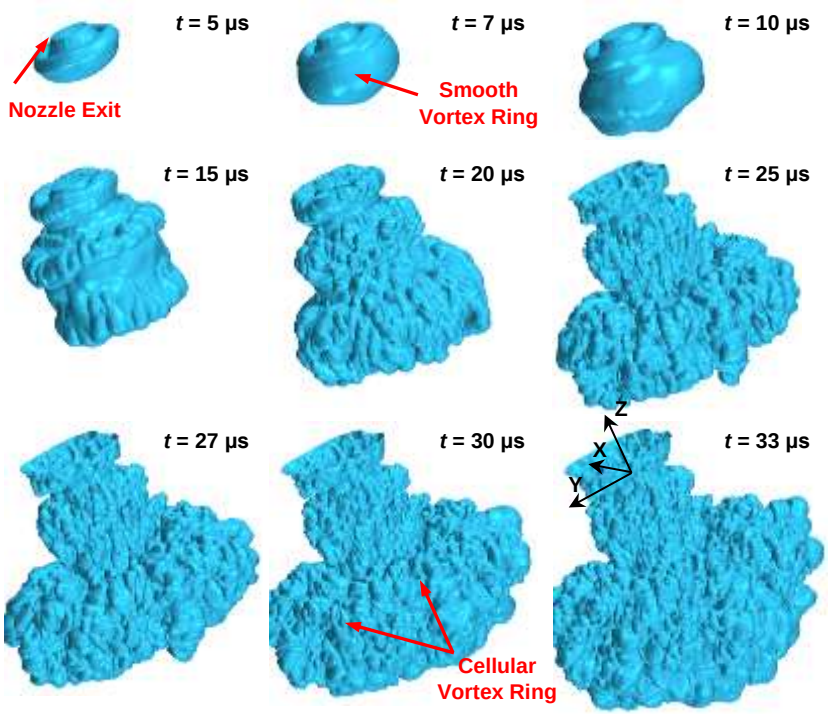

Figure 20. Three-dimensional visualisation of the preliminary vortex ring in the under-expanded hydrogen jet with P_∞=10 bar T_∞=600 K.

3.3.3 Parametric Study

Maximum jet tip and centreline penetrations of both hydrogen and methane jets injected into T_∞=600 K are plotted in **Figure 21**. For both jets the deviation of the maximum tip penetration from that on the centreline was found to occur almost simultaneously with the start of the smooth to cellular transition of the vortex ring (see **Figure 16**). For hydrogen, the deviation of these two penetration measures occurred earlier due to faster transition of the vortex ring to cellular status. **Figure 21** also shows that the difference between the maximum tip penetration and the centreline penetration of the hydrogen jet was greater than that quantified for methane. This may be attributed to both relatively higher turbulence and higher velocity magnitude within the hydrogen jet that resulted in larger levels of fluctuation at the boundaries.

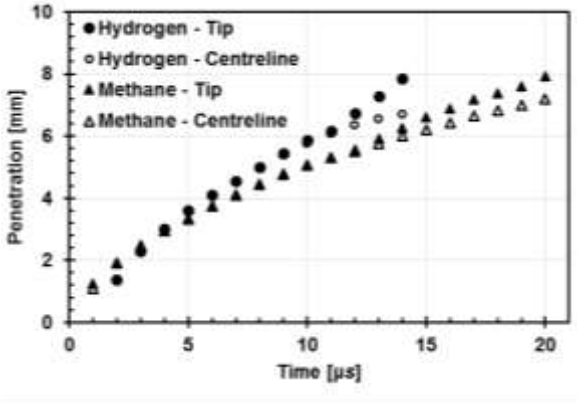

Figure 21. Maximum tip and centreline penetrations of the under-expanded hydrogen and methane jets P_∞=10 bar T_∞=600 K.

Figure 22 shows on the left the change in diameter of the preliminary vortex rings over time for both methane and hydrogen jets. This vortex ring diameter was measured as the distance between the left and right vortex cores on a 2D vertical plane similar to that of **Figure 16**. It is clear that the diameter increased

rapidly during the early stages of its formation, *i.e.* up to t≈10 and 15 μs for hydrogen and methane, respectively. This was attributed to the high radial velocity magnitude during the early stages of the expansion process that consequently resulted in large lateral angles between the edge of the embedded shock and the nozzle symmetry axis. This angle reduced gradually as the jets penetrated into the domain (see **Figure 17**). As shown in **Figure 22**, for the early stage of the vortex ring development, the trade-off between increasing circulation of the tip vortex over time and reducing the aforementioned lateral angle of the shock edge created a growing trend of the vortex diameter with negative rate. The preliminary vortex ring of the hydrogen jet vanished before t≈20 μs, while for methane it grew in diameter. Within t≈15–25 μs, the vortex ring diameter of the methane jet experienced a rapid increase with positive rate. The timing of 15 μs may be assumed as an inflection point in the methane data series of **Figure 22**. This was attributed to the formation of a strong *Mach* reflection and its consequent supersonic shear layers. The vortices of the shear layer fed the vortex ring and enhanced its circulation power (Gharib *et al.*, 1998).

The trajectories of the preliminary vortex cores are plotted in **Figure 22** on the right for both hydrogen and methane. Up to a value of Z/D≈1.5 the trajectories of the two gases followed a similar trend. This showed the evolution of the initial laminar vortex rings. It should be noted that the relatively higher value of X/D in the case of hydrogen was due to its higher radial expansion compared to methane. Past the location of Z/D≈1.5 and until Z/D≈2.2 the vortex ring of the hydrogen jet grew rapidly in both axial and radial directions. However, for Z/D≈2.2 (close to the *Mach* reflection) the ring started merging with the shear layer. For methane's jet, past Z/D≈1.5 and until Z/D≈4.0, the vortex ring expanded fairly smoothly in both Z and X directions with slightly higher gradients towards the radial direction (X). Downstream of the location Z/D≈4.0 the vortex core of the methane jet exhibited a fluctuating behaviour which was a sign of the start of the pinch-off process.

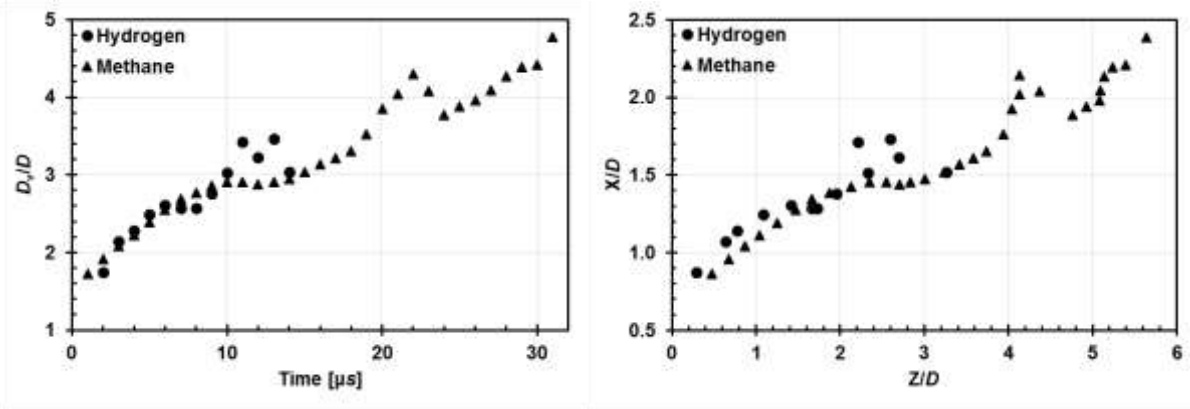

Figure 22. Variations of the initial vortex ring diameter with time (left) and trajectories of the preliminary vortex core (right) in the under-expanded hydrogen and methane jets with P_∞=10 bar and T_∞=600 K.

4. Conclusions

The present study used large eddy simulation in conjunction with an adaptive mesh refinement technique in order to investigate the mixing characteristics and three-dimensionality of the vortical structures in transient under-expanded hydrogen and methane jets under various ambient thermodynamic conditions, including both low and elevated ambient pressures and temperatures resembling in-cylinder states of gaseous-fuelled

IC engines with early or late injection strategies (NPR=10, P_∞≈1 and 10 bar, T_∞=296 and 600 K). Initially, extensive validation studies of the computational framework was conducted on the basis of three different experimental and computational test cases available in the literature. Additionally, direct comparison was performed between the mixing characteristics and vortical structures of hydrogen and methane jets issued into a fixed volume air-filled ambient with P_∞≈10 bar and T_∞=600 K. The main conclusions of the present study can be summarised as follows:

- At a constant ambient pressure and NPR, hydrogen jet injected into the hot ambient (T_∞=600 K) exhibited higher penetration length and volumetric growth (~21% and ~30% at t=30 μs, respectively) compared to the jet issued into the cold ambient (T_∞=296 K). This was mainly attributed to the lower density (and consequently lower resistance) of the hot ambient. The greater influence of ambient temperature rise on volumetric growth than on penetration can be attributed to the threefold increase in diffusivity that manifests itself more as an effect in the azimuthal direction since the flow is dominated by supersonic velocities axially.

- Under identical NPR and elevated ambient temperature and pressure, hydrogen exhibited significantly higher penetration length and volumetric growth compared to methane. Specifically, at t=30 μs, the hydrogen jet exhibited ~16% and ~117% higher penetration and volumetric growth.

- Methane injected into hot ambient showed noticeably lower volumetric growth in comparison to hydrogen jets issued into both cold and hot environments at the same ambient pressure and NPR. This was attributed to the relatively lower radial expansion of the methane jet, mainly due to its fairly lower molecular diffusivity and weaker vortex ring.

- A scaling coefficient for the volumetric growth of under-expanded jets was proposed. The newly proposed parameter takes into account differences in diffusivity, ratio of specific heats and ambient density and consequently can be used for direct comparison between under-expanded jets of different gases or issued into different ambient thermodynamic states.

- Flow separation at the edge of the embedded shock (to satisfy the *Kutta* condition) was shown to be the main cause of the initial tip rolling-up of the under-expanded jets and formation of the preliminary vortex rings.

- The preliminary vortex ring of both hydrogen and methane jets exhibited a smooth structure which turned cellular through a complex transient process. The transition from smooth to cellular vortex ring started ~8 μs earlier in the hydrogen jet than in the methane jet due to the relatively faster formation of the shear layers in the former jet. High level of shear in under-expanded jets form counter-rotating vortices within the jet volume and at the boundary of the jet with the ambient medium due to *Kelvin-Helmholtz* type instabilities which is believed to trigger the mixing and formation of the cellular structures.

- For under-expanded jets and, in particular, ‘bulky’ jets such as those of hydrogen, AMR should be considered as a technique for achieving an accurate representation of the entire jet volume, practically, only over specific time periods of the evolution of the jet, rather than a tool aimed to reduce computational costs in general over long jet penetration runs. This is because AMR can create extremely high number of cells within very short jet penetration lengths. Specifically, for a hydrogen jet with NPR=10 issued into an engine-like ambient condition, AMR produced over 23.5 M cells for a penetration length of $Z_t \approx 15$ mm (in ~30 μs of flow time) when solving the flow with a spatial resolution of $D/50$.

Acknowledgements

The authors acknowledge the use of University College London’s Legion High Performance Computing Facility (Legion@UCL), and associated support services, in the completion of this work.

REFERENCES

André B., Castelain T., and Bailly, C. (2014) Investigation of the mixing layer of underexpanded supersonic jets by particle image velocimetry. *International Journal of Heat and Fluid Flow*, 50, 188–200.

Antepara O., Lehmkuhl O., Borrell R., Chiva J., and Oliva A. (2015) Parallel adaptive mesh refinement for large-eddy simulations of turbulent flows. *Computers and Fluids*, 110, 48–61.

Cho H.M., He B., (2007) Spark ignition natural gas engines–a review, *Energy Conversion and Management*, 48, 608–618.

Cussler EL, (2009) Diffusion: mass transfer in fluid systems. 3rd Edition, *Cambridge University Press*.

Dauptain A., Cuenot B. and Gicquel Y.M., (2010) Large-eddy simulation of a stable supersonic jet impinging on flat plate, *AIAA Journal*, 48, 2325–2337.

Donaldson C. DuP. and Snedeker R.S., (1971) A study of free jet impingement. part 1. mean properties of free and impinging jets. *Journal of Fluid Mechanics*, 45, 281–319.

Edgington-Mitchell D., Honnery R.D. and Soria J., (2014) The underexpanded jet *Mach* disk and its associated shear layer, *Physics of Fluids*, 26, 096101.

Ferziger J.H., Peric M., (2002) Computational methods for fluid dynamics, *Springer*.

Gharib M., Edmond R. and Karim S., (1998) A universal time scale for vortex ring formation, *Journal of Fluid Mechanics*, 360, 121–140.

Golub V.V., (1994) Development of shock wave and vortex structures in unsteady jets, *Shock Waves*, 3,279–285.

Hamzehloo A. and Aleiferis, P.G., (2013) Computational study of hydrogen direct injection for internal combustion engines, *SAE Technical Paper* 2013-01-2524.

Hamzehloo A. and Aleiferis, P.G., (2014a) Numerical modelling of mixture and combustion in DISI hydrogen engines with various injection strategies, SAE Technical Paper 2014-01-2577.

Hamzehloo A. and Aleiferis, P.G., (2014b) Large eddy simulation of highly turbulent under expanded hydrogen and methane jets for gaseous-fuelled internal combustion engines, *International Journal of Hydrogen Energy*, 39, 21275–21296.

Hamzehloo A. and Aleiferis P.G., (2014c) Large eddy simulation of near-nozzle shock structure and mixing characteristics of hydrogen jets for direct-injection spark-ignition engines, *10th International Conference on Heat Transfer, Fluid Mechanics and Thermodynamics (HEFAT2014)*, Orlando, Florida, USA.

Hamzehloo A. and Aleiferis, P.G., (2016a) Gas dynamics and flow characteristics of highly turbulent under-expanded hydrogen and methane jets under various nozzle pressure ratios and ambient pressures, *International Journal of Hydrogen Energy*, 41, 6544–6566.

Hamzehloo A. and Aleiferis P.G., (2016b) On the Characteristics of shear layers vortical structures in highly under-expanded hydrogen and methane jets, *Flow, Turbulence and Combustion*, (submitted).

Hirschfelder J.O., Curtiss C.F. and Bird R.B. (1964) Molecular theory of gases and liquids. 2nd Ed. *John Wiley & Sons*.

Hornung H., (1986) Regular and Mach reflection of shock waves, *Annual Review of Fluid Mechanics*, 18, 33–58.

Inman J.A., Danehy P.M., Nowak R.J. and Alderfer D.W., (2008) Identification of instability modes of transition in underexpanded jets, *38th Fluid Dynamics Conference and Exhibit*, Seattle, Washington, USA, AIAA Paper 2008-4389.

Krothapalli A., Strykowski P.J. and King C.J., (1998) Origin of streamwise vortices in supersonic jets, *AIAA Journal*, 36, 869 – 872.

Liou M.S., (2006) A sequel to AUSM, Part II: AUSM $^{+}$-up for all speeds, *Journal of Computational Physics*, 214, 137–170.

Mitran, S.M. (2001) A comparison of adaptive mesh refinement approaches for large eddy simulation. *Washington University Seattle department of applied mathematics*, 397– 408.

Nicoud F. and Ducros F., (1999) Subgrid-scale stress modelling based on the square of the velocity gradient tensor, *Flow, Turbulence and Combustion*, 62, 183–200.

Ouellette P., Hill P.G., (2000) Turbulent transient gas injections, *Journal of Fluid Engineering*, 122(4), 743–753.

Owston R, Magi V, Abraham J, (2009) Fuel-air mixing characteristics of DI hydrogen jets. *SAE Int J Engines*, 1(1), 693–712.

Pack D.C., (1950) A note on Prandtl's formula for the wave-length of a supersonic gas jet, *The Quarterly Journal of Mechanics and Applied Mathematics*, 3, 173–181.

Pantano C., Deiterding R., Hill D.J., and Pullin D.I. (2007) A low numerical dissipation patch-based adaptive mesh refinement method for large-eddy simulation of compressible flows. *Journal of Computational Physics*, 221(1), 63–87.

Petersen B.R. and Ghandhi J.B., (2006) Transient high-pressure hydrogen jet measurements, *SAE Technical Paper 2006-01-0652*.

Pope S.B, (2000) Turbulent flows, *Cambridge University Press*.

Pope S.B., (2004) Ten questions concerning the large-eddy simulation of turbulent flows. *New journal of Physics*, 6(35).

Prudhomme S. M., Haj-Hariri H, (1994) Investigation of supersonic underexpanded jets using adaptive unstructured finite elements, Finite Elements in Analysis and Design, 17, 21–40.

Rogers T., Petersen P., Koopmans L., Lappas P. and Boretti A., (2015) Structural characteristics of hydrogen and compressed natural gas fuel jets, *International Journal of Hydrogen Energy*, 40, 1584–1597.

Ruggles A.J. and Ekoto I.W., (2012) Ignitability and mixing of underexpanded hydrogen jets, *International Journal of Hydrogen Energy*, 37, 17549–17560.

Scarcelli R., Wallner T., Matthias N., Salazar V. *et al.*, (2011) Mixture formation in direct injection hydrogen engines: CFD and optical analysis of single- and multi-hole nozzles, *SAE International Journal Engines*, 4(2), 2361–2375.

Thangadurai M. and Das D., (2010) Characteristics of counter-rotating vortex rings formed ahead of a compressible vortex ring, *Experiments in Fluids*, 49, 1247–1261.

Yu J., Vuorinen V., Kaario O., Sarjovaara T. and Larmi M., (2013) Visualization and analysis of the characteristics of transitional underexpanded jets, *International Journal of Heat and Fluid Flow*, 44, 140–154.

Velikorodny A, Kudriakov S. (2012) Numerical study of the near-field of highly underexpanded turbulent gas jets, *International Journal of Hydrogen Energy*, 37, 17390–17399.

Verhelst S., (2014) Recent Progress in The use of hydrogen as a fuel for internal combustion engines, *International Journal of Hydrogen Energy*, 39, 1071–1085.

Vuorinen V., Yu J., Tirunagari S., Kaario O., Larmi M., *et al.*, (2013) Large-eddy simulation of highly underexpanded transient gas jets, *Phys. Fluids*, 25, 016101.

Vuorinen V., Wehrfritz A., Duwig C. and Boersma B. J., (2014) Large-eddy simulation on the effect of injection pressure and density on fuel jet mixing in gas engines, *Fuel*, 130, 241–250.

Weiss J.M., Maruszewski J.P. and Smith W. A., (1999) Implicit solution of preconditioned Navier–Stokes equations using algebraic multigrid, *AIAA Journal*, 37, 29–36.

Weiss J.M. and Smith W.A., (1995) Preconditioning applied to variable and constant density flows, *AIAA Journal*, 33, 2050–2057.

White T, Milton B, (2008) Shock wave calibration of under expanded natural gas fuel jets, *Shock Waves*, 18, 353–364.

Zhang H., Chen Z., Li B and Jiang X., (2014) The secondary vortex rings of a supersonic underexpanded circular jet with low pressure ratio, *European Journal of Mechanics B/Fluids*, 46, 172 –180.